Micromechanical Modeling of Reinforcement Fracture in Particle-Reinforced Metal-Matrix Composites

M. FINOT, Y.-L. SHEN, A. NEEDLEMAN, and S. SURESH

Finite element analyses of the effect of particle fracture on the tensile response of particle-reinforced metal-matrix composites are carried out. The analyses are based on two-dimensional plane strain and axisymmetric unit cell models. The reinforcement is characterized as an isotropic elastic solid and the ductile matrix as an isotropically hardening viscoplastic solid. The reinforcement and matrix properties are taken to be those of an Al-3.5 wt pct Cu alloy reinforced with SiC particles. An initial crack, perpendicular to the tensile axis, is assumed to be present in the particles. Both stationary and quasi-statically growing cracks are analyzed. Resistance to crack growth in its initial plane and along the particle-matrix interface is modeled using a cohesive surface constitutive relation that allows for decohesion. Variations of crack size, shape, spatial distribution, and volume fraction of the particles and of the material and cohesive properties are explored. Conditions governing the onset of cracking within the particle, the evolution of field quantities as the crack advances within the particle to the particle-matrix interface, and the dependence of overall tensile stress-strain response during continued crack advance are analyzed.

I. INTRODUCTION

METALS reinforced with particles or short fibers of ceramics exhibit a variety of failure modes during the application of monotonic or cyclic loads: (a) fracture of the reinforcing ceramic, (b) ductile failure by the nucleation, growth, and coalescence of voids within the metallic matrix, and (c) delamination and crack growth along the interface between the matrix and the reinforcement. An understanding of the micromechanics of these failure processes is essential for improving the mechanical performance of metal-matrix composites that are currently being used or intended for use in a number of engineering applications.

It is now experimentally well documented that fracture of the reinforcing particle is one of the principal failure mechanisms in metal-matrix composites. A number of independent research studies[16-25] have identified the following general trends associated with particle fracture.

(1) The propensity for particle fracture increases with increasing reinforcement concentration.
(2) The propensity for particle fracture increases with increasing overall plastic strain.
(3) In the same tensile test specimen, larger particles fracture more easily than smaller ones.
(4) Regions of the composite with clustered reinforced particles exhibit a greater degree of particle fracture than regions where the local concentration of the particles is more dilute.
(5) Cracks within the reinforcement are usually oriented

normal to the loading axis for uniaxial tension, and parallel to the loading axis for uniaxial compression.
(6) The tendency for reinforcement failure depends on such factors as the reinforcement geometry and shape, matrix and reinforcement composition, interface properties, and thermomechanical processing techniques (such as extrusion).
(7) Defects that are introduced to the reinforcing phase during processing may serve as preferential nucleation sites for failure during subsequent mechanical loading.
(8) The damage introduced in the composite as a consequence of particle fracture can also trigger or influence other failure modes. For example, sharp microcracks that develop as a result of particle fracture can enhance localized ductile plastic flow within the matrix, thereby promoting such additional failure mechanisms as ductile separation by void growth or shear banding.
(9) Experiments show that particle fracture (a) decreases the overall stiffness, flow strength, and ductility of the composite, (b) decreases the total life in low-cycle fatigue, and (c) increases the apparent crack propagation rates in high-cycle fatigue.

Experimental work involving acoustic emission monitoring of particle failure, in situ scanning microscopy of evolving particle damage, X-ray tomography, and statistical analyses of particle fracture distribution have been reported in the literature for metal-matrix composites. Furthermore, finite element simulations of particle failure are being employed in greater numbers to gain an understanding of the overall mechanical response. For example, Shen et al[1] carried out a numerical analysis of the effects of reinforcement fracture on the overall elastic response of two-phase composites. They found that, for circular cylindrical reinforcements with an aspect ratio of unity (termed a unit cylinder) and a reinforcement-to-matrix Young's modulus ratio, E_R/E_M, of three, the decrease in Young's modulus of the composite due to the fracture of all the particles is just about evenly matched by the increase in stiffness arising from

M. FINOT and Y.-L. SHEN, formerly Graduate Research Assistants, Brown University, are Graduate Research Assistant and Postdoctoral Research Associate, respectively, Department of Materials Science and Engineering, Massachusetts Institute of Technology, Cambridge, MA 02139. A. NEEDLEMAN, Professor of Engineering, is with the Division of Engineering, Brown University, Providence, RI 02912. S. SURESH, Richard P. Simmons Professor of Materials Science and Engineering and Professor of Mechanical Engineering, is with the Massachusetts Institute of Technology, Cambridge, MA 02139.

the presence of the hard particle in a soft matrix. When $E_R > 3E_M$, the composite (with a penny-shaped crack at the center of each unit cylinder reinforcement particle) exhibits a stiffening effect. The effects of reinforcement fracture on the overall tensile plastic deformation of the metal-matrix composite have been studied theoretically by Bao[2] and Tvergaard.[3] In the former case, a three phase damage model was used, which allows for the study of the effects of limited reinforcement fracture on the effective stress-strain response, for perfectly bonded interfaces. In the latter study, an axisymmetric unit cell model was used specifically to address the interaction between reinforcement failure and matrix-reinforcement interfacial debonding in ceramic-whisker-reinforced metals. In these prior studies, the progression of particle failure and its effects on the development of field quantities within the matrix (as the crack within the particle advances to the interface and into the matrix) have not been explored.

In this article, the effects of particle fracture on the overall stress-strain response of the composite are examined in detail, along with the evolution of stress and strain fields within the particle and the matrix. We also present the results of finite-element analyses of the quasi-static progression of particle fracture into the interface and the ductile matrix. The analyses have been carried out within the context of axisymmetric and plane strain unit cell formulations. The model system chosen for study is an aluminum alloy reinforced with SiC particles. Experiments to quantify the extent of particle failure during tension loading have also been conducted on the aluminum-SiC composite in an attempt to develop a basis for the numerical models. The numerical simulations examine the onset of cracking within the particle, the evolution of field quantities as the crack advances within the particle to the interface with the matrix, and the dependence of overall constitutive response and matrix plastic deformation during continued crack advance within the matrix. Some specific cases of interfacial debonding are also considered.

II. NUMERICAL MODELING

The analyses are based on a convected coordinate Lagrangian formulation of the field equations, with the initial unstressed state taken as reference. All field quantities are considered to be functions of convected coordinates, y^i, and time, t. The region under consideration consists of two phases, the matrix and the reinforcement, with allowance made for the possibility of separation across specified surfaces in the matrix and in the reinforcement as well as for the possibility of interfacial decohesion. The principle of virtual work is written as[4,5]

$$\int_V \tau^{ij} \delta E_{ij} dV - \int_{S_{int}} T^i \delta \Delta_i dS = \int_S T^i \delta u_i dS \qquad [1]$$

Here, τ^{ij} are the contravariant components of the Kirchhoff stress ($\tau = J\sigma$, where σ is the Cauchy stress and J is the ratio of current to reference volume of a material element) on the deformed convected coordinate net. The quantities V and S are the volume and external surface,

respectively, of the body in the reference configuration, S_{int} is the cohesive surface area, and Δ_i are the covariant components of the displacement jump across the cohesive surface. Across a perfectly bonded surface $\Delta_i \equiv 0$.

The nominal traction components, T^i, and the Lagrangian strain components, E_{ij}, are given by

$$T^i = (\tau^{ij} + \tau^{kj}u^i_{,k})\nu_j \qquad [2]$$

$$E_{ij} = \frac{1}{2}(u_{i,j} + u_{j,i} + u^k_{,i}u_{k,j}) \qquad [3]$$

where ν is the surface normal in the reference configuration, u_j are the covariant components of the displacement vector on base vectors in the reference configuration, and $(\ )_{,i}$ denotes covariant differentiation in the reference frame.

Composite response is analyzed using both plane strain and axisymmetric cell models. For the plane strain analyses, a Cartesian reference frame is used with the $y^1 - y^2$-plane being the plane of deformation, while in the axisymmetric calculations, the reference frame is cylindrical with the identifications $y^1 = r$, $y^2 = z$, and $y^3 = \theta$. As discussed by Tvergaard,[6] the axisymmetric cell model is an approximation to a three-dimensional array of hexagonal cylinders. The aggregate is subject to axial straining and free to contract laterally so that the rate boundary conditions on the cell are

$$\dot{u}_2 = \dot{U}_2 = \dot{\varepsilon}_{ave}(L_0 + U_2), \qquad \dot{T}^1 = 0 \quad \text{on } y^2 = L_0 \qquad [4]$$

$$\dot{u}_1 = \dot{U}_1, \qquad \dot{T}^2 = 0 \quad \text{on } y^1 = R_0 \qquad [5]$$

Here, $(\dot{\ }) = \partial(\ )/\partial t$, $\dot{\varepsilon}_{ave}$ is a prescribed constant, and U_1 is determined from the condition that the average lateral traction rate vanishes; i.e.,

$$\int_0^{L_0} \dot{T}^1 dy^2 = 0 \quad \text{on } y^1 = R_0 \qquad [6]$$

On $y^1 = 0$,

$$\dot{u}_1 = 0, \qquad \dot{T}^2 = 0 \qquad [7]$$

In the axisymmetric calculations, the conditions in Eq. [7] are along the symmetry axis, whereas in the plane strain analyses Eq. [7] is imposed to enforce symmetry of the cell deformations about $y^1 = 0$.

For presentation of the results, we define the overall strain, the overall average axial stress, and the average axial stress in the reinforcement as

$$\varepsilon_{ave} = \int_0^t \dot{\varepsilon}_{ave} dt \qquad [8]$$

$$\Sigma_{ave} = \frac{1}{V_{cell}} \int_{V_{cell}} (\tau^{22} + \tau^{k2}u^2_{,k})dV \quad \text{and} \qquad$$

$$\Sigma_R = \frac{1}{V_R} \int_{V_R} (\tau^{22} + \tau^{k2}u^2_{,k})dV \qquad [9]$$

where V_{cell} is the cell volume (unit thickness is assumed in the plane strain analyses) and V_R is the reinforcement volume.

We allow for the possibility of an initial central crack

along $y^2 = 0$. In the axisymmetric analyses, the initial crack is penny shaped with radius a, and in the plane strain analyses, the initial crack half-length is denoted by a. Along the crack surface,

$$\dot{T}^1 = \dot{T}^2 = 0 \quad \text{on } 0 \leq y^1 < a \qquad [10]$$

The crack is constrained to propagate along $y^2 = 0$. Resistance to crack growth in its plane of propagation, as well as particle-matrix decohesion, is modeled using a cohesive surface constitutive relation that is a phenomenological mechanical relation between the traction and displacement jump across the surface. In both cases, the cohesive constitutive relation is taken to be elastic, with the reactions derived from a potential ϕ that only depends on the components of the displacement jump across the surface, Δ_i,

$$T^i = -\frac{\partial \phi}{\partial \Delta_i} \qquad [11]$$

With n^i and t^i denoting components of unit vectors normal and tangential to the cohesive surface, and defining normal, $\Delta_n = n^i u_i$, and tangential, $\Delta_t = t^i u_i$, displacement jumps, the potential ϕ is taken to have an exponential form[7] that allows for tangential as well as normal decohesion.

$$\phi(\Delta_n, \Delta_t) = \phi_n + \phi_n \exp\left(-\frac{\Delta_n}{\delta_n}\right)\left\{\left[1 - r + \frac{\Delta_n}{\delta_n}\right]\frac{1-q}{r-1}\right.$$
$$\left. - \left[q + \left(\frac{r-q}{r-1}\right)\frac{\Delta_n}{\delta_n}\right]\exp\left(\frac{\Delta_t^2}{\delta_t^2}\right)\right\} \qquad [12]$$

where

$$q = \frac{\phi_t}{\phi_n} \qquad r = \frac{\Delta_n^*}{\delta_n} \qquad [13]$$

The cohesive length parameters δ_n and δ_t are defined by

$$\phi_n = \sigma^{\max} e \delta_n, \qquad \phi_t = \sqrt{\frac{e}{2}} \tau^{\max} \delta_t \qquad [14]$$

where $e = \exp(1)$, and ϕ_n and $\sigma^{\max}$ are the work of separation and the strength, respectively, for normal separation; ϕ_t and $\tau^{\max}$ are the corresponding quantities for tangential separation. The cohesive parameter Δ_n^* is the value of Δ_n after complete shear separation with zero normal tension.

With increasing separation, the magnitude of the traction at first increases, reaches a maximum, and then approaches zero. The key parameters are the stress required for separation and the length scale over which separation occurs. Cracklike behavior is obtained when all geometric dimensions are large relative to the cohesive characteristic lengths δ_n and δ_t. In the limit of mode I cracklike behavior, the initiation of growth is characterized by $J = \phi_n$, where J is Rice's [27] J integral. The limiting case of perfect bonding corresponds to $\sigma^{\max} \to \infty$ and, along the particle-matrix interface, $\tau^{\max} \to \infty$. However, here when perfect bonding is enforced, it is modeled directly by imposing displacement continuity across the interface.

Subsequently, three different cohesive surfaces are considered, in the reinforcement, in the matrix, and along the particle matrix interface with cohesive parameters denoted by $(\ )_R$, $(\ )_M$, and $(\ )_{int}$, respectively. Symmetry along $y^2 = 0$ requires that $T^t = T^1 = 0$ there. Along the path of crack propagation through the particle and into the matrix $r = q = 0$ (with $\delta_t \neq 0$) so that $T^1 \equiv 0$ on $y^2 = 0$. Thus, only the normal decohesion parameters, denoted by $\sigma_R^{\max}$, δ_R and $\sigma_M^{\max}$, are used to specify the reinforcement and matrix cohesive surfaces. We emphasize that in this cohesive surface formulation,[4,5] crack initiation and crack growth are calculated directly in terms of the material properties and of the parameters characterizing the cohesive surface separation law; no ad hoc fracture criterion is imposed.

The matrix material is characterized as an isotropically hardening elastic viscoplastic solid, and the total rate of deformation, $\mathbf{D}$, is written as the sum of an elastic part, $\mathbf{D}^e$, (small elastic strains are assumed) and a plastic part $\mathbf{D}^p$, with

$$\mathbf{D}^e = \frac{1+\nu}{E}\hat{\boldsymbol{\tau}} - \frac{\nu}{E}(\hat{\boldsymbol{\tau}}:\mathbf{I})\mathbf{I} \qquad [15]$$

$$\mathbf{D}^p = \frac{3\dot{\varepsilon}}{2\sigma}\boldsymbol{\tau}' \qquad [16]$$

where $\hat{\boldsymbol{\tau}}$ is the Jaumann rate of Kirchhoff stress, $\mathbf{I}$ is the identity tensor, $\mathbf{A}:\mathbf{B}$ denotes $A^{ij}B_{ji}$, $\dot{\bar{\varepsilon}}$ is the effective strain rate, E is Young's modulus, and ν is Poisson's ratio, and

$$\sigma_h = \frac{1}{3}\boldsymbol{\tau}:\mathbf{I}, \qquad \boldsymbol{\tau}' = \boldsymbol{\tau} - \sigma_h\mathbf{I}, \qquad \bar{\sigma}^2 = \frac{3}{2}\boldsymbol{\tau}':\boldsymbol{\tau}' \qquad [17]$$

$$\dot{\bar{\varepsilon}} = \dot{\varepsilon}_0[\bar{\sigma}/g(\bar{\varepsilon})]^{1/m},$$
$$g(\varepsilon) = \sigma_0(\bar{\varepsilon}/\varepsilon_0 + 1)^N, \qquad \varepsilon_0 = \sigma_0/E \qquad [18]$$

Here, $\bar{\varepsilon} = \int \dot{\bar{\varepsilon}}dt$ and the function $g(\bar{\varepsilon})$ represents the effective stress vs effective strain response in a tensile test carried out at a strain rate such that $\dot{\bar{\varepsilon}} = \dot{\varepsilon}_0$. Also, σ_0 is a reference strength that for the nearly rate-independent response modeled here is effectively the yield strength; N and m are the strain-hardening exponent and strain-rate-hardening exponent, respectively.

The model composite system studied is an Al-3.5 wt pct Cu alloy matrix reinforced with SiC particles. The material properties are derived from a thermomechanical processing history that produces the peak hardness level in the matrix.[8,9,10] The properties of the matrix material are taken to be $E = 71.8$ GPa, $\nu = 0.33$, $\sigma_0 = 175$ MPa, $N = 0.2$, and $m = 0.004$, and in the numerical modeling, these parameter values are regarded as characterizing the Al-3.5 wt pct Cu alloy. The SiC reinforcement is modeled as a linear elastic solid with $E = 450$ GPa and $\nu = 0.17$.

Standard identities, see e.g. Hutchinson[11] and Needleman,[12] are used to phrase the constitutive relation [15] and [16] in terms of the contravariant components of the convected derivative of Kirchhoff stress, $\hat{\tau}^{ij}$, and the Lagrangian strain-rate components, $\dot{E}_{ij}$, where E_{ij} is defined in Eq. [3]. This relation is then substituted into the rate form of Eq. [1] to obtain the variational

equation that is the basis of the finite element discretization.

The discretizations are carried out using quadrilateral elements, each of which is composed of four "crossed" linear displacement triangles. The incremental boundary value problem is solved using a combined finite element Rayleigh–Ritz method.[13] The deformation history is calculated in a linear incremental manner, and in order to increase the stable time step, the rate tangent modulus method of Peirce et al.[14] is used. Representative finite element meshes are shown in Figure 1 for the reinforcement shapes considered in the analyses. Figures 1(a) and (b) show mesh arrangements used for unit cylinder reinforcement (or unit square reinforcement in the plane strain calculations) and Figure 1(c) shows a mesh for a truncated cylinder reinforcement. The mesh in Figure 1(b) is used for numerical convenience and efficiency when cohesion of the particle-matrix interface is modeled by Eqs. [11] to [14]. The mesh configuration in Figure 1(b) gives a slight rounding of the sharp corner in Figure 1(a), which does not substantially affect the results presented here. Typically, finite element meshes with between 576 and 1024 elements were used in the calculations. In several cases, convergence of the solution was checked. For example, in one case, increasing the number of elements in the reinforcement cohesive surface by a factor of two resulted in a less than 2 pct change in the calculated strain to failure.
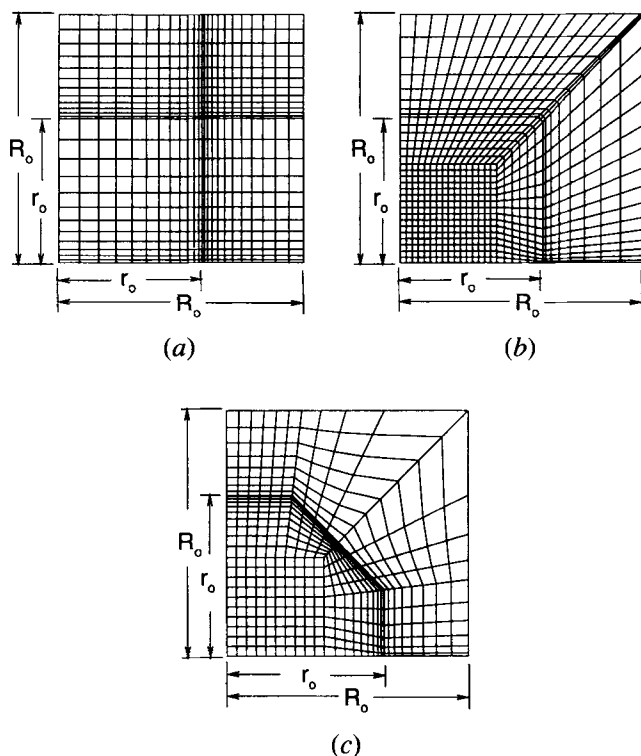

(a)

(b)

(c)

Fig. 1 — Representative unit cell quadrants and finite element meshes used for (a) a unit cylinder reinforcement with a perfectly bonded particle-matrix interface; (b) a unit cylinder reinforcement with the cohesion of the particle-matrix interface described by Eqs. [11] through [14]; and (c) a truncated cylinder reinforcement. Other meshes have been used to refine the mesh near the initial crack tip. Each quadrilateral consists of four crossed linear displacement triangles.

III. EXPERIMENTAL OBSERVATIONS

In the present work, uniaxial tensile tests were conducted on specimens of the model material system, viz., Al-3.5 wt pct Cu with SiC particle reinforcements, with the purpose of (a) demonstrating that particle fracture is the principal damage mechanism during uniaxial tensile deformation (and thereby providing an experimental justification for the numerical simulations), (b) illustrating the overall features of particle fracture in the model system, and (c) developing guidelines for the choice of parameters and failure criteria in the numerical simulations. The majority of the tensile tests were conducted on an Al-3.5 wt pct Cu alloy with 20 vol pct of SiC particles; some experiments were also done on the Al-3.5 wt pct Cu alloy with 13 vol pct of SiC particles. The SiC particles, with an aspect ratio of close to unity, were irregularly shaped with sharp corners. Full details of tensile specimen geometry and orientation, as well as details of the microstructure, processing, and thermomechanical heat treatments for the composites, can be found elsewhere.[8,9,10]

The following procedure was used for performing the tensile experiments. The specimens were subjected to a predetermined amount of applied uniaxial tensile strain following which the imposed loads were removed. In the unloaded state, the gage section of the specimen was examined in an optical/scanning microscope to document the extent of damage, particularly particle fracture. The specimens were then reloaded in the tensile testing machine to a greater magnitude of applied tensile strain and then were examined again in the microscope for particle damage in the unloaded condition. This procedure was repeated until final fracture occurred. A large number of micrographs representing a statistically significant sample of the gage section were gathered after each interruption of the tensile test, in an attempt to determine quantitatively the extent of particle fracture. The tensile tests were also repeated in duplicate specimens to check for reproducibility of results.

Figure 2(a) is a scanning electron micrograph of the lateral surface within the gage section of the tensile specimen, taken after failure at a strain of 0.03, in the aluminum alloy with 20 vol pct SiC particles. This figure clearly shows that particle fracture is the primary damage mechanism in the composite during uniaxial tensile deformation. Larger particles appear to fracture much more easily than smaller ones. In this and subsequent micrographs, the principal direction of cracking in the particles is normal to the tensile axis. Figure 2(b) shows a different specimen where a dominant crack nucleated within a SiC particle has advanced into the matrix. Note here the residual blunting of the crack in the unloaded state. The direction of crack growth is macroscopically normal to the tensile loading axis. In addition to particle fracture, ductile failure by void growth within the matrix was also observed in the present tests. (Detailed numerical simulations of ductile failure by the growth and coalescence of voids within the matrix of the Al-SiC composites were presented in earlier articles,[8,9] and this mechanism will not be considered further in the present article.) To a relatively lesser extent, interfacial debonding was also visible in the micrographs. Some special cases of interfacial debonding, which accompanies
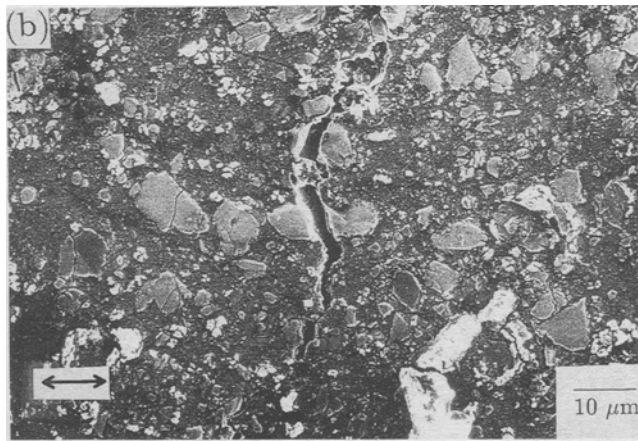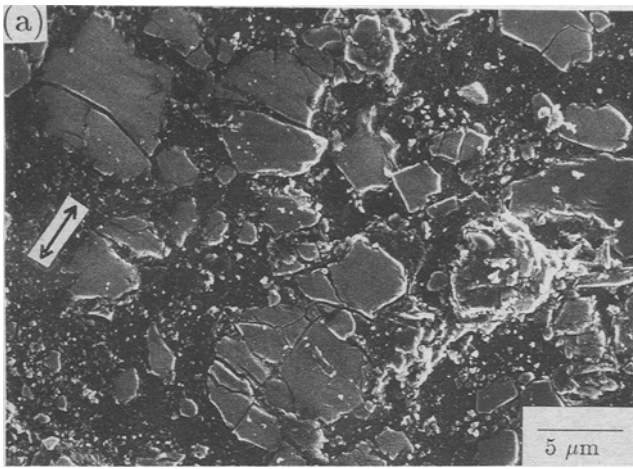
Fig. 2—(a) and (b) Micrographs illustrating various damage modes in a 20 pct-SiC reinforced Al-3.5 wt pct Cu alloy: particle fracture and crack advance into the matrix. The arrows indicate the tensile loading axis.
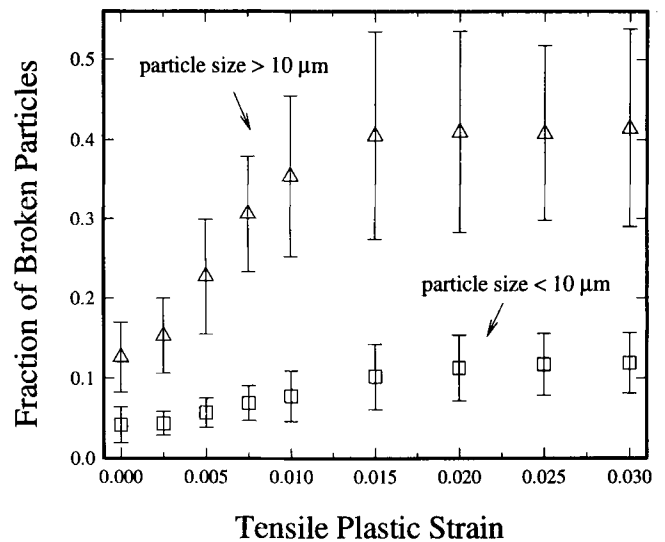

Fig. 3—Fraction of broken particles as a function of tensile plastic strain for two ranges of reinforcement size for a 20 pct-SiC particle-reinforced Al-3.5 wt pct Cu alloy.

particle fracture, are considered in Sections V and VI of this article.

The influences of particle size and imposed strain on the propensity for particle fracture are illustrated in Figure 3. Here, the fraction of broken particles (i.e., the number of broken particles divided by the total number of particles within the area of observation for a given particle size range) is plotted as a function of the residual tensile plastic strain from the interrupted tensile tests conducted on the Al-3.5Cu alloy with 20 vol pct SiC particles. The fraction of large broken particles (of size greater than 10 μm) is approximately three times greater than that of smaller particles (of size between 4 and 10 μm). The scatter in the experimental data on the number of fractured particles is also smaller for the smaller particles. For both size ranges, the fraction of broken particles reaches a saturation value at a residual plastic strain of about 0.015 and remains essentially unchanged until final fracture. Similar trends were also observed for the Al-Cu alloy reinforced with 13 vol pct SiC particles.

The experimental results obtained in this work are similar to those reported by other researchers who have employed a variety of techniques, including in situ optical microscopy[16,17] and SEM,[26] X-ray micro-tomography,[18] and acoustic emission,[19] to quantify

particle fracture in Al-SiC composites. The conclusions of all these experimental studies can be collectively summarized as follows:

(1) The fraction of fractured particles, f_c, increases with the size of the reinforcing particle at a fixed applied strain ε_{ave}.
(2) f_c increases with the volume fraction of reinforcing particles at fixed ε_{ave}.
(3) The fracture plane within the particle is normal to the applied load in tension and parallel to the loading direction in compression.
(4) f_c for a given particle size increases with ε_{ave} until a critical value of ε_{ave} beyond which it remains unchanged.
(5) Particle fracture appears to be the primary damage mechanism when the matrix alloy is of high purity and the interface between the matrix and the reinforcement is strongly bonded. However, the advance of the crack from within the ceramic particle into the ductile matrix can promote ductile failure by the nucleation, growth, and coalescence of voids. This mechanism can become prominent when the matrix contains a large fraction of such void-nucleating particles as intermetallic inclusions and dispersoids (see Llorca et al.[8,9] for further details).
(6) In the present work, a limited amount of interfacial debonding has also been observed, ostensibly due to the local stress intensification as the crack in the particle intersects the interface and causes blunting within the ductile matrix.
(7) Processing-induced defects within the particles serve as preferential sites for the nucleation of cracks during loading.[20]
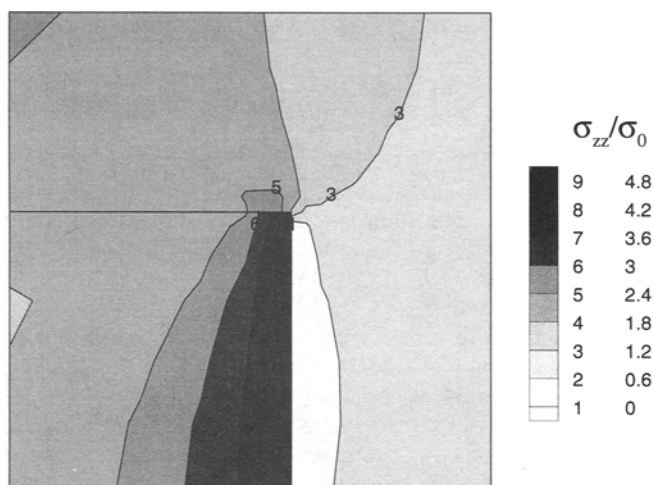
IV. PARAMETRIC ANALYSES

A mechanistic rationale for the general features of the experimental results can be provided by finite element simulations that explore the effects of various geometric and loading parameters on the propensity for particle
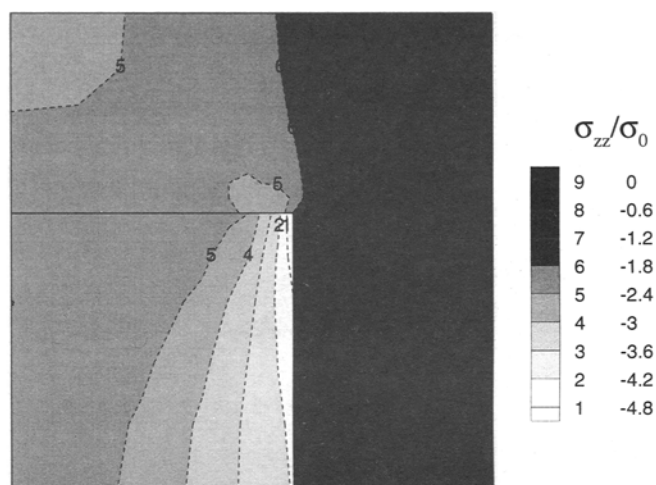
fracture. In this section, we discuss numerical simulations of the evolution of field quantities within the particle and the matrix, in an attempt to establish a link between the evolution of local stress fields and the macroscopic trends associated with particle fracture. For all the simulations discussed in this section, the particle is assumed to be intact (no initial crack) and the particle-matrix interface is taken to be perfectly bonded; modeling of particle cracking and its effects on composite response is taken up in Sections V and VI.

Cracks introduced within particles during mechanical loading are generally found to be perpendicular to the loading axis under uniaxial tension and parallel to the loading axis under uniaxial compression.[15,22,23] In Figures 4 through 6, an axisymmetric model with unit cylinder reinforcement is considered, subject to uniaxial loading parallel to the cylinder axis. Figures 4(a) and (b) show contour plots of the physical components of axial stress (denoted by σ_{zz}) and lateral stress (σ_{rr}) in the cell
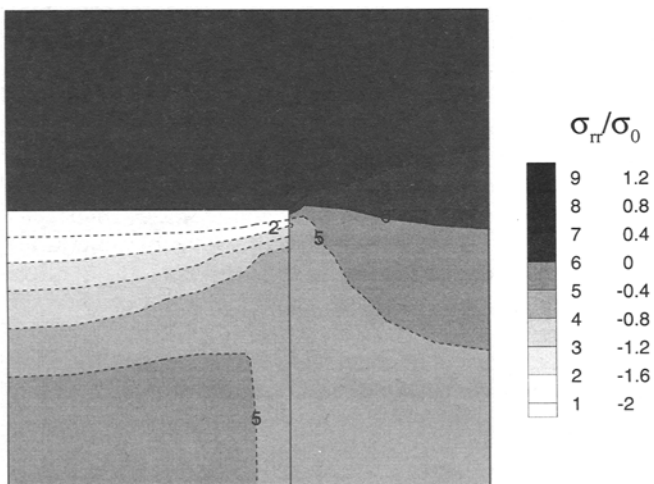
quadrant at $\varepsilon_{ave} = 0.005$ for the Al 3.5 Cu + 20 vol pct SiC composite. (The strain $\varepsilon_{ave} = 0.005$ corresponds to an early stage of gross plastic deformation of the composite.) The corresponding plots for compressive loading are shown in Figures 5(a) and (b). In Figure 4, tensile loading results in tensile axial stresses and compressive lateral stresses within the cylindrical particle. The stress magnitudes are greater in the reinforcement than in the matrix, with the largest stress magnitudes in the matrix occurring above the particle. There is a peak radial stress in Figure 4(b) that is in the matrix between particles. Compressive loading (Figure 5) results in the same features but with stress components of opposite sign. Presuming that the normal tensile stress is mainly responsible for reinforcement cracking and that cracking occurs perpendicular to the tensile axis, Figures 4 and 5 show the expected tendency for cracking perpendicular to the loading axis in tension and parallel to the loading axis in compression.
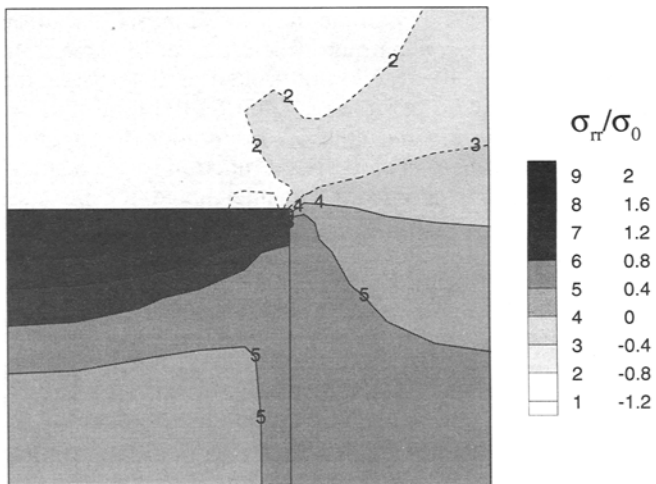

(a)

	σ_{zz}/σ_0	
9	4.8
8	4.2
7	3.6
6	3
5	2.4
4	1.8
3	1.2
2	0.6
1	0

(b)

	σ_{rr}/σ_0	
9	1.2
8	0.8
7	0.4
6	0
5	-0.4
4	-0.8
3	-1.2
2	-1.6
1	-2

Fig. 4—Computed contour plots of (a) the physical axial stress component, σ_{zz}, and (b) the physical lateral stress component, σ_{rr}, for the Al-3.5 wt pct Cu alloy reinforced with 20 vol pct axisymmetric unit cylinder particles, at $\varepsilon_{ave} = 0.005$. The tensile axis is in the vertical direction. The stress values are normalized by the matrix strength, σ_0.

(a)

	σ_{zz}/σ_0	
9	0
8	-0.6
7	-1.2
6	-1.8
5	-2.4
4	-3
3	-3.6
2	-4.2
1	-4.8

(b)

	σ_{rr}/σ_0	
9	2
8	1.6
7	1.2
6	0.8
5	0.4
4	0
3	-0.4
2	-0.8
1	-1.2

Fig. 5—Computed contour plots of (a) the physical axial stress component, σ_{zz}, and (b) the physical lateral stress component, σ_{rr}, for the Al-3.5 wt pct Cu alloy reinforced with 20 vol pct axisymmetric unit cylinder particles, at $\varepsilon_{ave} = -0.005$. The loading axis is in the vertical direction. The stress values are normalized by the matrix strength, σ_0.

Figures 6(a) and (b) show contour plots of constant maximum principal stress for the 13 and 20 pct reinforced materials, respectively, $\varepsilon_{ave} = 0.005$. The maximum principal stress field within the particle is very similar to the corresponding axial stress field, as can be seen by comparing Figures 6(a) and 4(a). Figure 6 reveals that the maximum principal stresses within the particle are higher for the composite with 20 pct reinforcement than for the composite with 13 pct reinforcement. This is consistent with the experimental observation that particle fracture tends to increase with reinforcement volume fraction.

In metal-matrix composites, variations in reinforcement size and spatial distribution are typical. Such *local* variations in particle size and spatial arrangement can have a strong bearing on the local occurrence of particle fracture. In order to illustrate that local variations in reinforcement size and distribution can markedly influence the principal stresses within the particle (for fixed loading and with all other parameters fixed), thereby affecting the propensity for particle fracture, we consider two periodic unit cell arrangements within the context of a plane strain formulation with square reinforcements. Each of these arrangements consists of two sizes of SiC particles in the Al-3.5Cu matrix, with the side length of the larger particle being twice that of the smaller one. Figure 7(a) is a schematic of the first arrangement, hereafter referred to as configuration ⟨a⟩, wherein the smaller particles are located at the center of a square unit cell packed by the larger particles or *vice versa*. In this arrangement, the centers of the smaller particles are not aligned with those of the larger ones. Figure 7(b) is a schematic of the second arrangement, hereafter referred to as configuration ⟨b⟩, wherein the centers of the smaller and larger particles are aligned.

Figures 8(a) and (b) show contour plots of constant maximum principal stress for configurations ⟨a⟩ and ⟨b⟩ respectively, at $\varepsilon_{ave} = 0.005$. It is seen that for configuration ⟨a⟩, the maximum principal stress values in the larger particle are significantly greater than those in the smaller one. However, in configuration ⟨b⟩, comparable stress values occur in the larger and smaller particles.

One reason that there is a greater tendency for the larger particles to fracture is because the probability of finding a pre-existing crack greater than some critical flaw size is greater for larger particles. Our results show that, in addition, for certain particle distributions, the stress tending to propagate a suitably oriented initial crack is also greater in larger particles than it is in smaller particles. In Figure 7, when the smaller particle is not aligned with the large one along the applied loading direction, the large particle has a higher maximum principal stress (configuration ⟨a⟩).

As noted in Section III, experiments show that the propensity for reinforcement fracture is higher in regions where the particles are clustered. Since particle clustering gives a higher local particle volume fraction, this leads to high stress levels within the clustered particles, which promotes particle fracture.

V. FRACTURE WITHIN A PARTICLE

In this section, crack growth is simulated with Eqs. [11] to [14], describing the resistance to crack
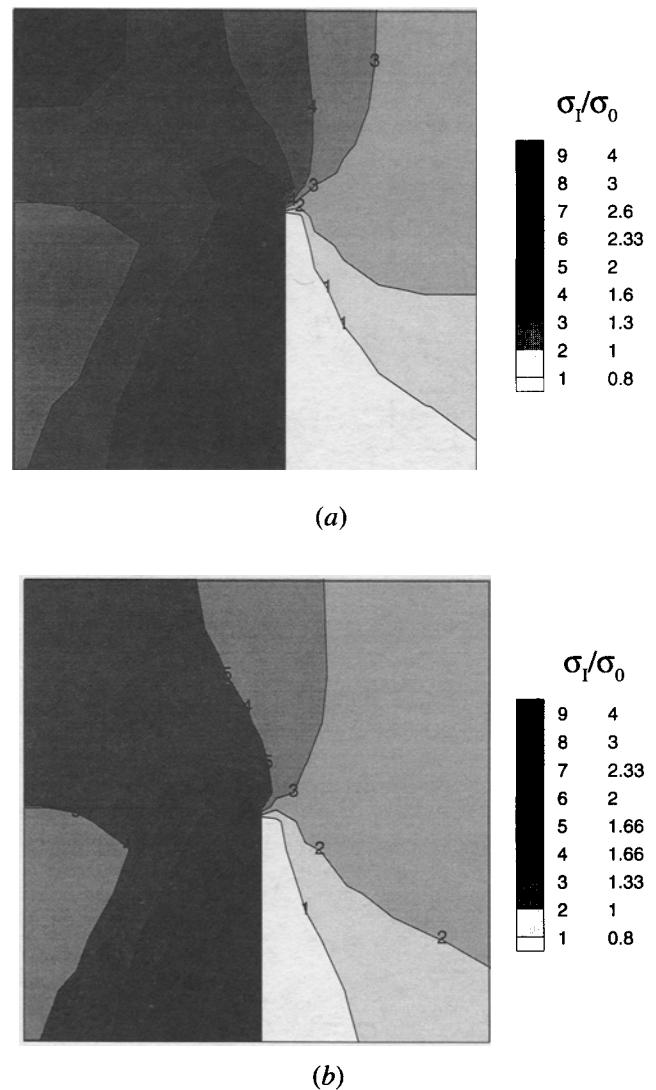
(*a*)

(*b*)

Fig. 6—Computed contour plots of maximum principal stress at $\varepsilon_{ave} = 0.005$ for the Al-3.5 wt pct Cu alloy reinforced with (*a*) 20 vol pct and (*b*) 13 vol pct axisymmetric unit cylinder particles. The tensile axis is in the vertical direction. The stress values are normalized by the matrix strength, σ_0.

growth. All calculations are carried out using an axisymmetric unit cell model for a uniform distribution of particles of aspect ratio unity. The volume fraction of reinforcement is fixed at 20 pct and the shape of the reinforcement is taken to be either a unit cylinder, Figure 1(b), or a truncated cylinder, Figure 1(c). For the unit cylinder, $r_0/R_0 = 0.58$, and for the truncated cylinder, $r_0/R_0 = 0.65$.

An initial penny-shaped crack introduced during processing, is assumed present at the center of the particle and the propagation of this pre-existing crack through the particle toward the matrix is simulated, with attention confined to crack growth within the reinforcement. The effects of the mechanical properties of the constituent phases, the initial crack size, and the shape of the inclusion on crack growth are analyzed. In these simulations, an unrealistically small value is used for the reinforcement cohesive strength, σ_R^{max}, for convenience in exploring qualitative features of the response. Smaller values of σ_R^{max} lead to less sharp stress gradients at the
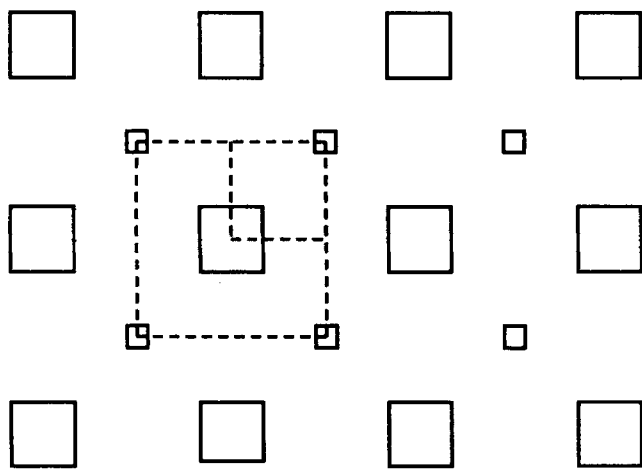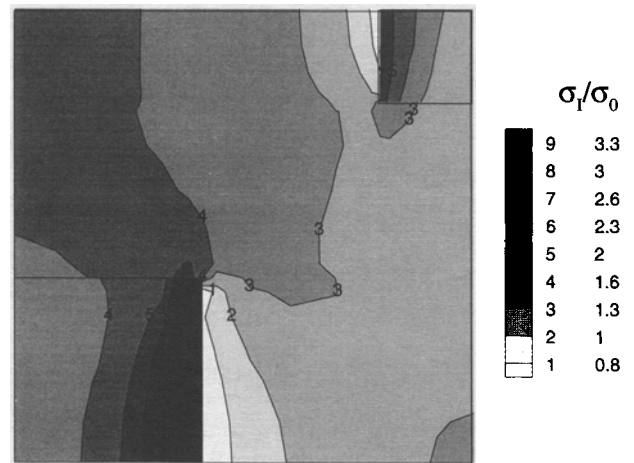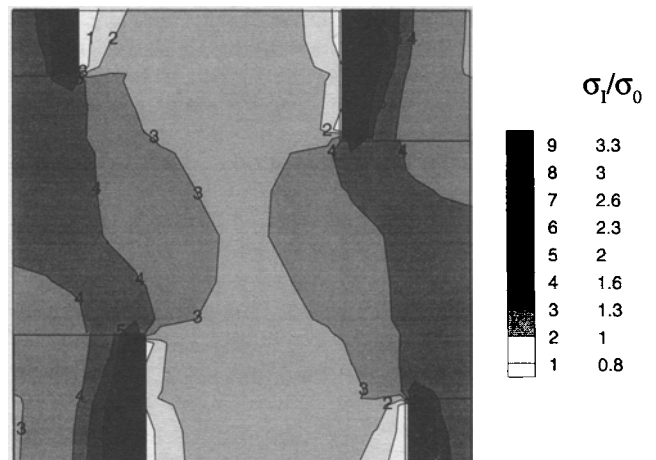
(a)
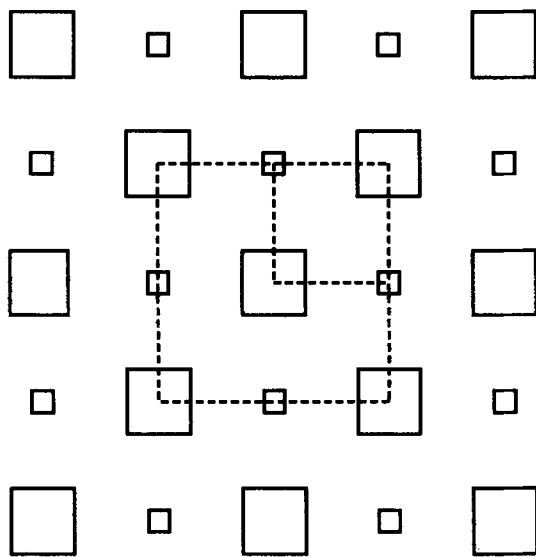
(b)

Fig. 7 — (a) and (b) Schematic diagrams showing two configurations, ⟨a⟩ and ⟨b⟩, respectively, of uniformly dispersed particles. Two particle sizes are assumed to exist in the composite. The dash lines represent the unit cells and the quadrants used for plane strain finite element modeling.

(a)

(b)

Fig. 8 — Computed contour plot of maximum principal stress for plane strain model composites with 20 area pct reinforcement at $\varepsilon_{ave} = 0.005$: (a) configuration ⟨a⟩ and (b) configuration ⟨b⟩. The loading axis is in the vertical direction. The stress values are normalized by the matrix strength, σ_0.

crack tip so that a coarser mesh can be used. However, the values of σ_R^{max} and δ_R used in the computations are chosen to give rise to particle fracture in the strain range seen experimentally in Figure 2. The effect of an increase in σ_R^{max} (with an associate decrease in δ_R) is considered in Section VI–B. In this section, unless specified otherwise, the characteristics of the particle-matrix interface are given by $\sigma_{int}^{max} = 500$ MPa, $\tau_{int}^{max} = 500$ MPa, $\delta_n^{int} = 0.00147\ R_0$, $\delta_t^{int} = 0.0045\ R_0$, and $r = 7$. The matrix cohesive surface parameters are taken to be $\sigma_M^{max} = 400$ MPa and $\delta_M = 0.0021\ R_0$. From Eq. [14], the corresponding values of the normal work of separation, ϕ_n, are $2 \times 10^6\ R_0$ and $2.28 \times 10^6\ R_0$ for the interface and matrix, respectively. For example, with $R_0 = 5\ \mu m$, $(\phi_n)_{int} = 10\ J/m^2$ and $(\phi_n)_M = 11\ J/m^2$.

Figure 9(a) shows the effect of varying matrix strength and strain hardening. The average axial stress within the reinforcement, Σ_R, is plotted as a function of the overall

strain, ε_{ave}, for cracked truncated cylinder particles with an initial crack length $a = 0.61 r_0$. The reinforcement cohesive strength is specified by $\sigma_R^{max} = 500$ MPa and $\delta_R = 0.00083 R_0$. For $\sigma_0 = 175$ MPa and $N = 0.2$, crack growth through the particle occurs at $\varepsilon_{ave} = 0.0095$. Increasing the matrix yield strength to 200 MPa, with N fixed, or increasing N, with σ_0 fixed, increases the average stress in the particle. As a consequence, the strain at which the crack grows through the particle is reduced to $\varepsilon_{ave} = 0.008$ and to $\varepsilon_{ave} = 0.0085$, respectively. Note that $\Sigma_R > 0$ after the particle has cracked through, because stress is still transmitted through the particle matrix interface. The results in Figure 9(a) show that the peak stress is essentially the same in all three cases so that a criterion for the maximum stresses carrying capacity of the particle based on a critical value of the average axial reinforcement stress Σ_R (or, almost equivalently, of the average maximum principal stress) would be a good approximation. For a whisker, this criterion may not hold, because of strong axial stress

gradients. Then, the criterion in Tvergaard,[3] which involves a critical value of the normal stress at a cross section (the symmetric plane of the reinforcement in Reference 3), could be used instead.

The effect of varying the compliance of the particle-matrix interface is shown in Figure 9(b). In one case, the particle-matrix interface is taken to be nearly perfectly bonded ($\sigma_{int}^{max} = \tau_{int}^{max} = 10$ GPa), whereas in the other case, the particle-matrix interface cohesive properties are as specified earlier in this section. These parameters are chosen so that the strength of the interface is large enough to prevent any debonding on the upper part of the particle prior to the crack growing completely through the particle. Increasing the interface compliance increases the value of the overall strain at which crack growth through the particle occurs and lowers the peak value of Σ_R slightly. The large drop in Σ_R in Figures 9(a) and (b) is associated with crack growth through the particle and a bit into the ductile matrix. Then, on the lower plateau, the crack remains stationary. In Figure 9(b), the drop in the Σ_R vs ε_{ave} curves around $\varepsilon_{ave} = 0.02$ is due to subsequent crack propagation in the ductile matrix and, eventually, complete propagation through the unit cell.

Figure 10 shows curves of aggregate average axial stress, Σ_{ave}, vs the imposed average strain ε_{ave} for three cases; (a) an intact particle, $a = 0.0$; (b) a particle that has an initial part-way-through crack, $a = 0.61r_0$; and (c) a particle that is initially cracked through, $a = r_0$. Here, σ_M^{max} is taken to be 800 MPa to prevent crack growth completely through the matrix and the particle matrix interface is nearly perfectly bonded ($\sigma_{int}^{max} = \tau_{int}^{max} = 10$ GPa). The reinforcement cohesive characteristics are specified by $\sigma_R^{max} = 1.0$ GPa and $\delta_R = 0.00041R_0$. The part-way-through crack only has a small effect on the overall composite stiffness until crack growth occurs. (Note that for the cell model here, this corresponds to every particle in the composite being cracked.) Once the crack begins to grow, it propagates through the particle at nearly constant overall strain (for higher values of σ_R^{max}, equilibrium solutions would only be available for decreasing ε_{ave}). Because of released elastic energy, Σ_{ave} falls below that for a particle that is initially cracked through. However, subsequently, as the crack grows into the matrix the response is very close to that for an initially cracked-through particle ($a = r_0$).

The plots of overall axial stress, Σ_{ave}, vs overall strain, ε_{ave}, in Figure 11 illustrate the effect of initial crack size. Initial penny-shaped crack radii of $0.31r_0$, $0.61r_0$, and r_0 are considered for the truncated cylinder and of $0.34r_0$, $0.69r_0$, and r_0 for the unit cylinder. The reinforcement cohesive strength is specified by $\sigma_R^{max} = 500$ MPa and $\delta_R = 0.00083R_0$. The values of Σ_R at the fracture of the reinforcement are equal to 310 and 425 MPa for the unit cylinder and equal to 360 and 420 MPa for the truncated cylinder for the two crack sizes, respectively. The course of crack growth is the same as for the case shown in Figure 9, although here, the overall axial stress Σ_{ave}, rather than the particle average axial stress, is plotted; the peak value of Σ_{ave} is associated with the initiation of crack growth in the particle, Σ_{ave} drops substantially as the crack grows through the particle and somewhat into the ductile matrix (the radius of the penny-shaped crack in this regime is $\approx 1.05r_0 - 1.10r_0$), the crack then remains stationary over a range of increasing strain. The second drop
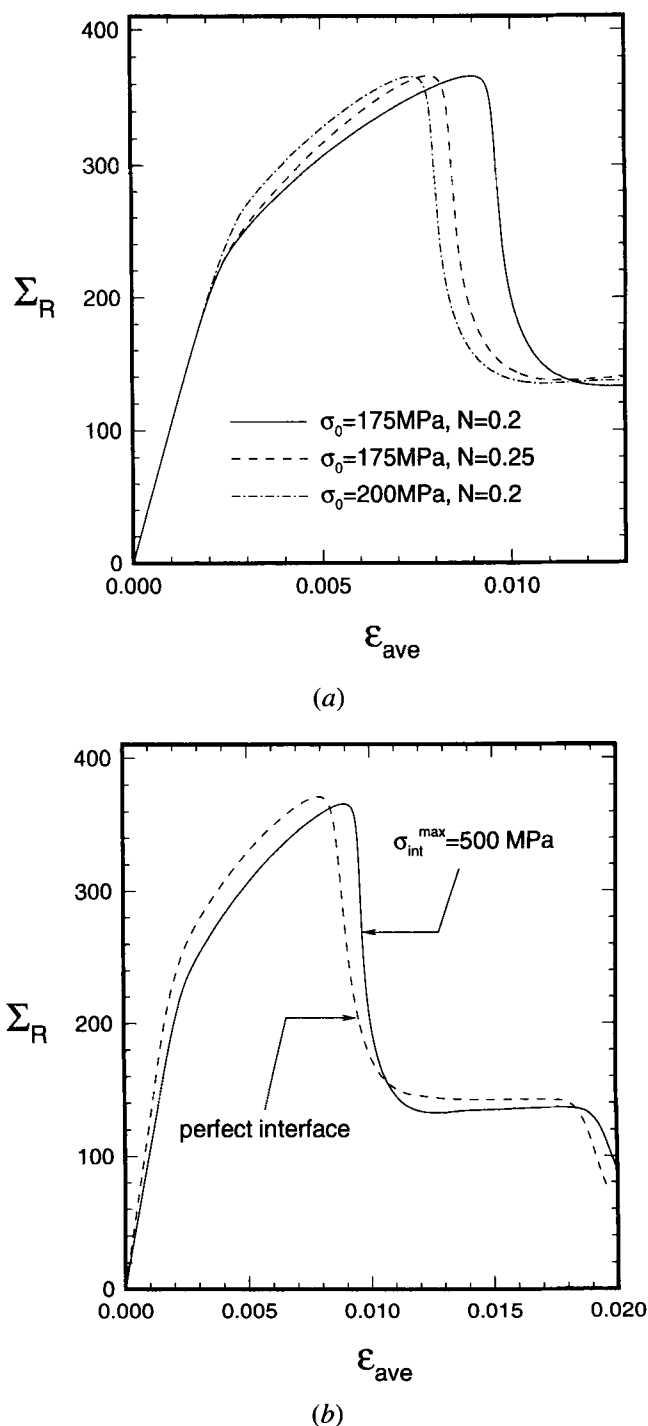

(a)

(b)

Fig. 9—Curves of average axial stress in the reinforcement, Σ_R (in MPa), vs imposed strain, ε_{ave}: (a) effect of variations in matrix strength and strain hardening and (b) effect of variations in strength of the particle-matrix interface (the perfect interface is simulated by taking $\sigma_{int}^{max} = \tau_{int}^{max} = 10$ GPa). The composite modeled is the Al-3.5 wt pct Cu alloy reinforced with 20 vol pct axisymmetric truncated cylinder particles. The radius of the initial penny-shaped crack is $a = 0.61\ r_0$.

in Σ_{ave} occurs when crack propagation resumes. Eventually, the crack grows through the unit cell and Σ_{ave} falls to zero. Both the initiation of crack growth and crack propagation through the reinforcement depend strongly on the initial size of the crack, which is due to the higher stress-intensity factor of a longer crack. Because the probability of finding a longer crack is greater in larger
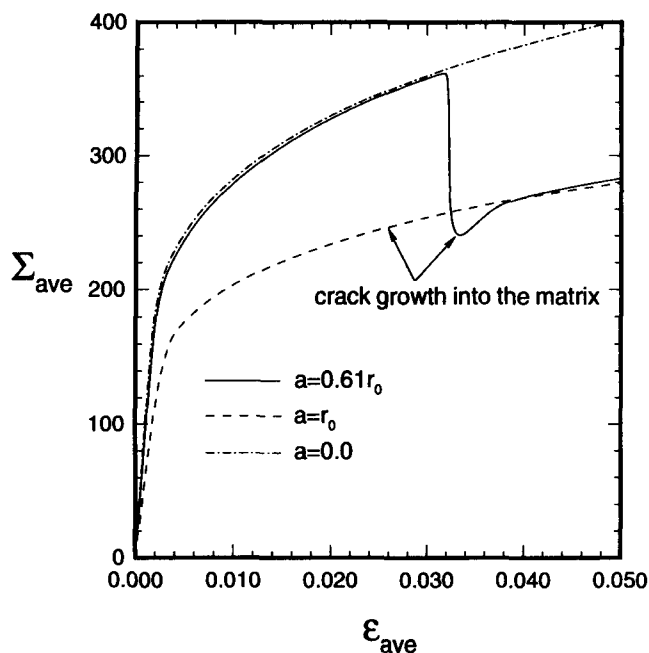
Fig. 10—Curves of overall axial stress, Σ_{ave} (in MPa), vs overall axial strain, ε_{ave}, showing the effect of crack growth on the overall stress strain response of the Al-3.5 wt pct Cu alloy reinforced with 20 vol pct axisymmetric truncated cylinder particles; $\sigma_R^{max} = 1.0$ GPa and $\delta_R = 0.00041$ R_0. The curve for $a = 0.0$ shows the response of a composite with all particles intact.

particles, the lower peak value of Σ_{ave} for larger initial cracks is consistent with the size effect on reinforcement fracture.

Previous studies have already revealed that reinforcement shapes with abrupt corners tend to increase the stress in the reinforcement significantly. A detailed comparison has been carried out for two different shapes: a truncated cylinder and a unit cylinder. In Figure 12, the radius of the initial penny-shaped crack is fixed at $a = 0.2R_0$, equivalent to $a = 0.31r_0$ for the truncated cylinder and $a = 0.34r_0$ for the unit cylinder. The reinforcement cohesive strength specified by $\sigma_R^{max} = 500$ MPa and $\delta_R = 0.00083R_0$. The computations reveal that crack growth through the unit cylinder occurs far earlier than for the truncated cylinder (Figure 12). For the truncated cylinder, reinforcement crack growth through the reinforcement occurs at $\varepsilon_{ave} = 0.015$ as compared with $\varepsilon_{ave} = 0.006$ for the unit cylinder. This is explained by the higher stress level in the cylindrical reinforcement in the plastic regime illustrated by the curve of Σ_R vs ε_{ave} in Figure 12.

The main qualitative features of these results are expected to hold for more realistic values of reinforcement strength, namely, that a criterion for particle fracture based on a critical average axial reinforcement stress or critical average maximum principal stress is a good approximation, with the critical value depending on the initial crack size and particle shape as well as on the reinforcement fracture strength. Taking, for example $\sigma_R = E_R/20$, with a correspondingly reduced value of δ_R to give comparable values of the work of separation, would require a much finer mesh than used here, and the computational resources needed would preclude carrying out parameter studies. This higher reinforcement cohesive strength would also lead to a *brittle* mode of decohesion so that crack

growth would occur dynamically, rather than quasi-statically. This point is discussed further in Section VI–B.

VI. EFFECT OF PARTICLE FRACTURE ON AGGREGATE TENSILE RESPONSE

A. Stationary Cracks within the Particle and Matrix

Figure 13 shows predicted aggregate axial stress strain curves with and without particle fracture for the Al-3.5 Cu alloy reinforce with 20 vol. pct SiC axisymmetric unit cylinder particles (Figure 1(a)) (the material properties are given in Section II). For comparison purposes, the experimental tensile stress-strain curve is also shown. The calculations are terminated at the fracture strain observed in the experiments. In the calculation with particle fracture, each particle is assumed to contain a stationary central penny-shaped crack with $a = r_0$ and, for both calculations in Figure 13 the particle-matrix interface is taken to be perfectly bonded. Particle fracture reduces the aggregate Young's modulus and flow strength, but the strain-hardening exponent is essentially unaltered by particle fracture. The experimentally measured stress-strain curve falls between the predictions for the intact and fractured particle calculations for values of ε_{ave} up to around 0.02. Beyond this strain, the experimental data fall below the numerical predictions, probably because the computations are for stationary cracks; crack propagation into the matrix is not accounted for in the calculations in Figure 13. In this regard, it is worth emphasizing that in the computation with cracked particles, all reinforcing particles in the composite are taken to be cracked so that the maximal effect of fixed length particle cracks is modeled. The stress drop associated with crack propagation from the particle into the matrix is suggestive of the possibility that progressive fracture might lead to an apparent change in the work-hardening rate (see the experimental data in Figure 13). The difference seen in the work-hardening rate between the predictions and experimental results in Figure 13 may well arise from the fact that the calculations in Figure 13 do not account for crack growth into the matrix. Furthermore, the model does not account for other failure mechanisms, such as ductile failure by void growth, which are known to occur in particle-reinforced aluminum alloys.

Figures 14 (a) and (b) show contours of mean normal stress σ_h, normalized by σ_0, and effective plastic strain $\bar{\varepsilon}$, respectively, at $\varepsilon_{ave} = 0.005$ for the calculation in Figure 13 with intact particles. The corresponding plots for the case with each particle cracked through ($a = r_0$) are shown in Figures 14(c) and (d). By comparing Figures 14(a) and (c), it is clear that particle fracture results in substantially reduced hydrostatic tension in the matrix. In Figure 14(c), high values of hydrostatic tension are confined to the vicinity of the crack tip, whereas for the intact particle in Figure 14(a), there is a large region above the reinforcement where the hydrostatic tension is large. Within the particle, very different distributions of mean normal stress are obtained with and without particle fracture. Also, in spite of the highly stressed regions in the cracked particle, the elastic strain energy in the cracked particle is 37.5 pct less than that
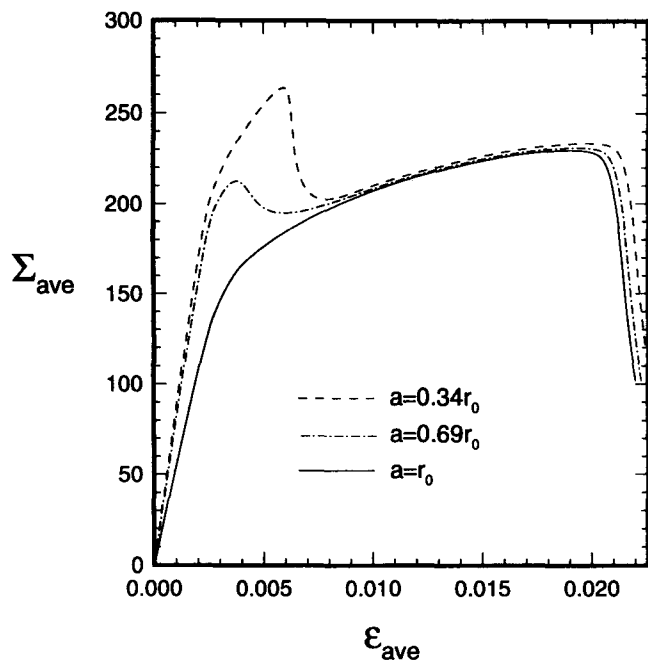
(a)
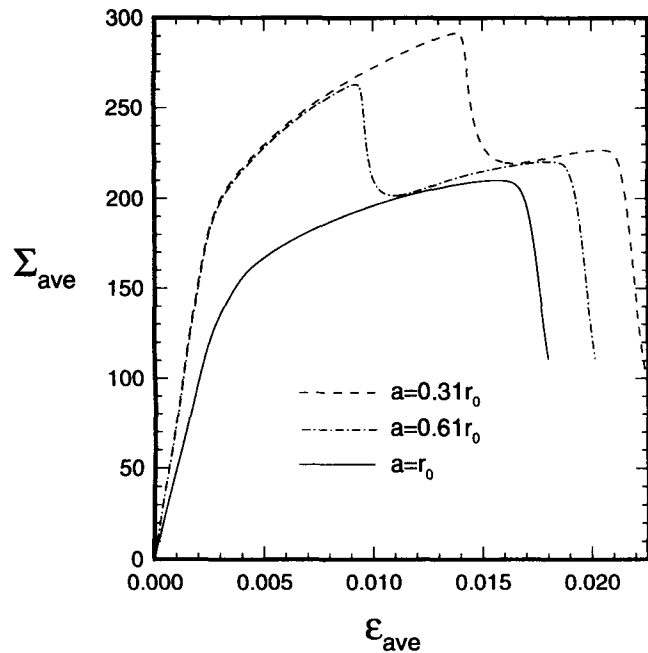
(b)

Fig. 11—Curves of overall axial stress, Σ_{ave} (in MPa), vs overall axial strain, ε_{ave}, showing the effect of initial crack size on the overall stress-strain response of the Al-3.5 wt pct Cu alloy with 20 vol pct reinforcement: (a) for a unit cylinder-shaped particle and (b) for a truncated cylinder-shaped particle. The cohesive properties of the reinforcement are $\sigma_R^{max} = 500$ MPa and $\delta_R = 0.00083 \, R_0$.

Fig. 12—Curves of average axial stress in the reinforcement. Σ_{ave} (in MPa), vs overall axial strain, ε_{ave}, showing the effect of particle shape for the Al-3.5 wt pct Cu alloy with 20 vol pct reinforcement and with all particle cracked. The initial radius of each penny-shaped crack is $a = 0.2R_0$ in both cases, which corresponds to $a = 0.34r_0$ for the unit cylinder and $a = 0.31r_0$ for the truncated cylinder.

Fig. 13—Curves of overall axial stress, Σ_{ave} (in MPa), vs overall axial strain, ε_{ave}, for the Al-3.5 wt pct Cu alloy reinforced with 20 vol pct axisymmetric unit cylinder particles, with all particles intact ($a = 0.0$) and with all particles cracked through ($a = r_0$). Also shown is an experimental stress-strain curve for the composite.

in the intact particle. Figures 14(b) and (d) show that the values of effective plastic strain, $\bar{\varepsilon}$, near the top-left corner of the cell quadrant and near the particle corner are much reduced for the cracked particle, although large plastic strains occur in the matrix near the crack tip.

In these analyses, a fractured particle was taken to contain a penny-shaped crack with its tip right at the interface. Figure 15 shows aggregate stress-strain curves
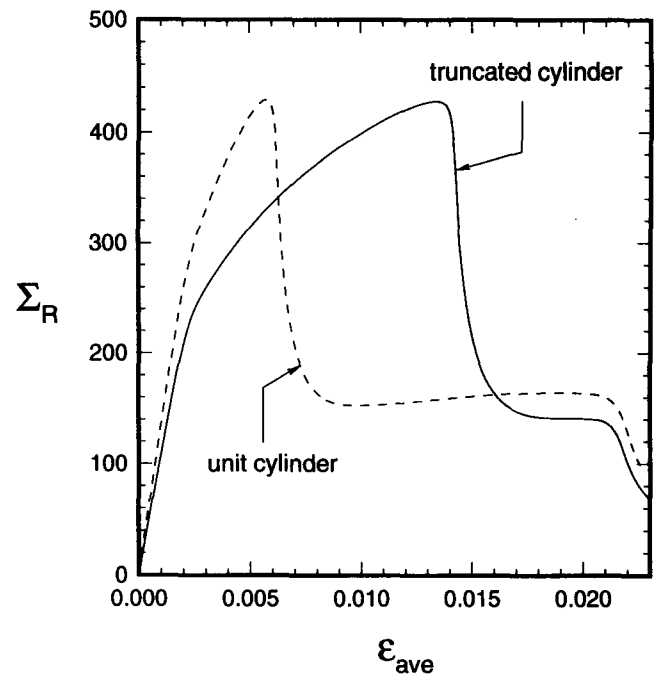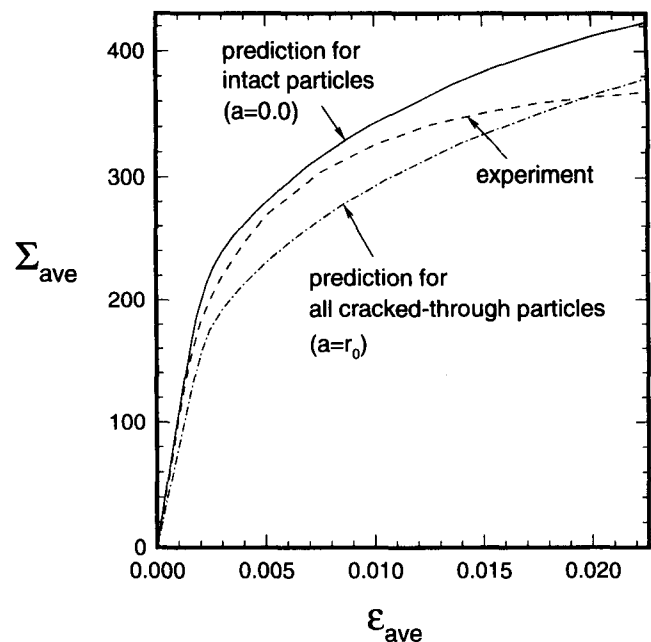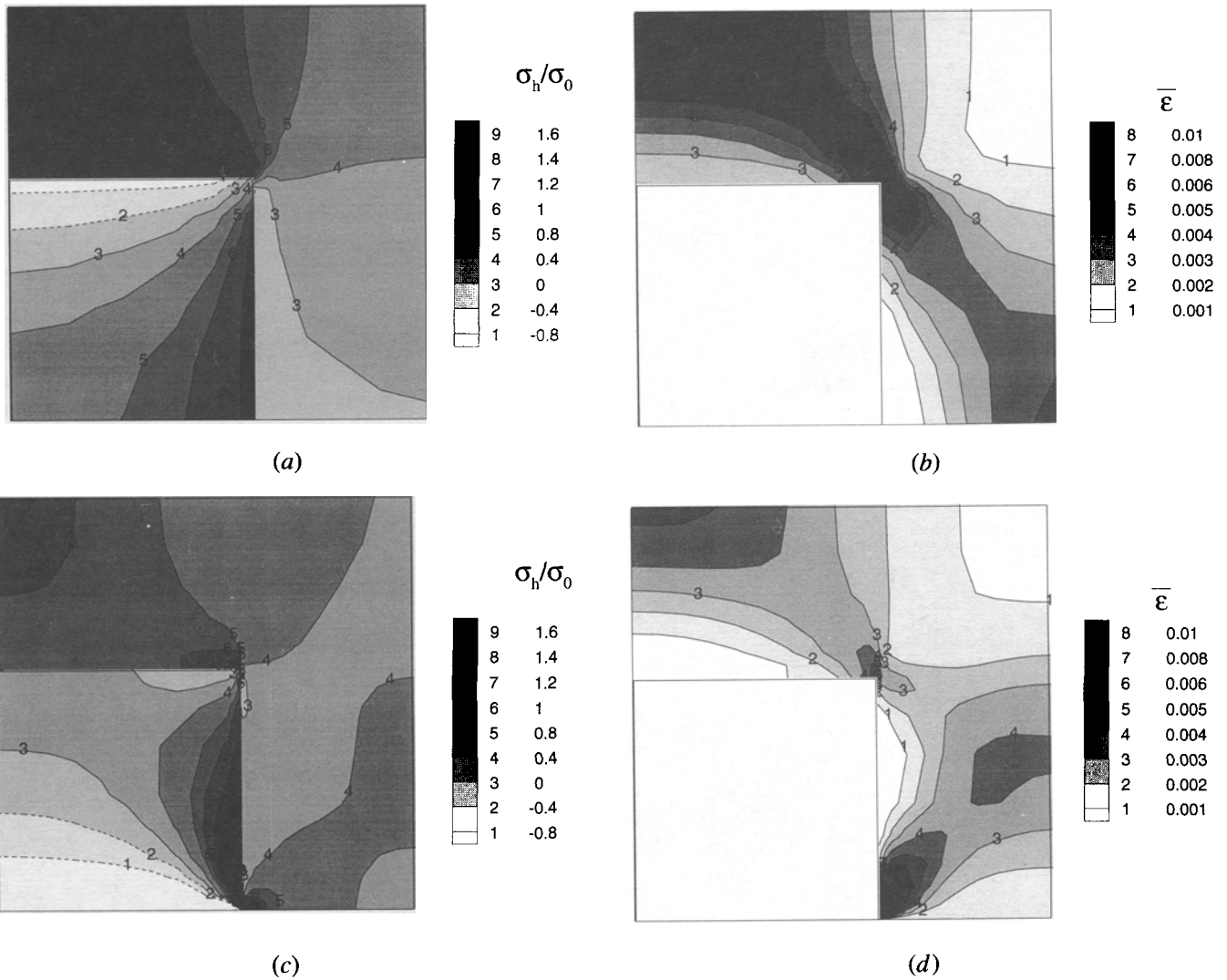
Fig. 14—Computed contour plots for the Al-3.5 wt pct Cu alloy reinforced with 20 vol pct unit cylinder particles at ε_{ave} = 0.005: (a) normalized mean normal stress, σ_h/σ_0, for intact particles (a = 0.0); (b) effective plastic strain ε, for intact particles (a = 0.0); (c) normalized mean normal stress, σ_h/σ_0, for fully cracked particles (a = r_0); and (d) effective plastic strain, $\bar{\varepsilon}$, for fully cracked particles (a = r_0). The tensile axis is vertical.

illustrating the effect of varying the size of the penny-shaped crack (as in Figure 13, the particle and matrix are taken to be perfectly bonded). The crack sizes considered span a range from being confined well inside the particle to extending far into the matrix. With $a = 0.25r_0$, there is only slight reduction in Σ_{ave} from the intact particle case (a = 0); even with $a = 0.75r_0$, the stress level is only decreased about 5 pct. However, the aggregate stress level falls sharply when the crack tip approaches the particle matrix interface. The most dramatic feature observed is the change between $a = r_0$ and $a = 1.001r_0$. The aggregate stress level decreases drastically when the crack tip is in the matrix. There is also a reduction in the aggregate strain-hardening rate. Note that the aggregate stress-strain response for $a = 1.001r$ falls below that of the pure matrix material. For larger cracks, the aggregate stress-carrying capacity decreases gradually. The lowest curve in Figure 15 shows the response for a crack that extends one fourth of the way through the surrounding matrix material.

Contour plots of mean normal stress, σ_h, and effective plastic strain, $\bar{\varepsilon}$, for $\alpha = 1.001r_0$ are shown in

Figures 16(a) and (b), respectively at ε_{ave} = 0.005. Comparing Figure 14(c), where $a = r_0$, with Figure 16(a) shows that the high hydrostatic tension in the particle, near the particle matrix interface, which occurs when $a = r_0$, is substantially reduced for $a = 1.001r_0$. Also, the hydrostatic tension in the matrix above the particle (when $a = r_0$) is partially relieved when the crack tip is in the matrix. Comparing Figures 14(d) and 16(b) shows that plastic deformation near the crack tip is enhanced when the crack tip is in the matrix. With $a = 1.001r_0$, deformation is focussed in a band (inclined about 45 deg from the tensile axis) eminating from the crack tip, whereas with $a = r_0$, deformation also occurs in a more or less orthogonal band intersecting the reinforcement corner.

The effect of matrix strain hardening is illustrated in Figure 17 that shows aggregate axial stress-strain curves for $a = r_0$ and $a = 1.001r_0$, with N = 1.0, 0.5, and 0.2 (N = 0.2 is used to characterize the matrix in Figure 15), with all other parameters fixed. The difference between the response with $a = r_0$ and with $a = 1.001r_0$ decreases with increasing N.
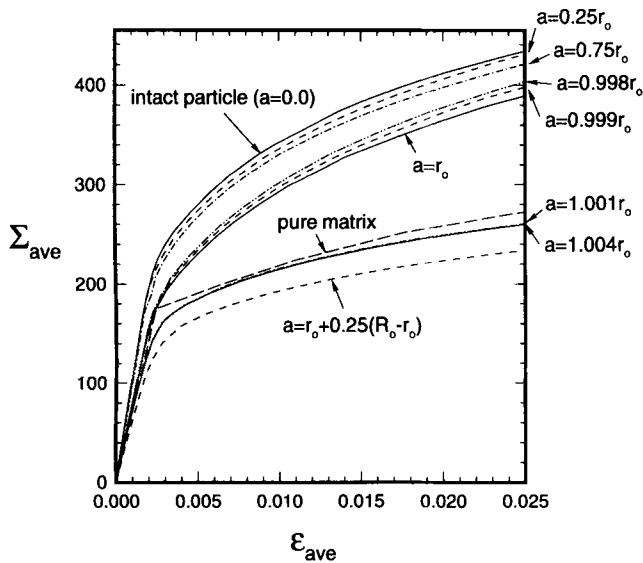
Fig. 15—Curves of overall axial stress, Σ_{ave} (in MPa), vs overall axial strain, ε_{ave}, for the Al-3.5 wt pct Cu alloy reinforced with 20 vol pct unit cylinder particles and with penny-shaped cracks in the particles of various initial radii. In the computations, the cracks are stationary. For comparison purposes, overall stress-strain curves are shown for a composite with intact particles ($a = 0.0$) and for the pure matrix material.

A plane strain cell model is used to explore the effect of having some, but not all, particles cracked. The unit cell has two equal-sized, diagonally arranged particles, as sketched in the insert to Figure 18 and with each particle perfectly bonded to the matrix. The aggregate stress-strain curves in Figure 18 are for an area fraction 0.2. Three cases are considered: all of the particles intact (0 pct), one of the particles cracked (50 pct), and all of the particles cracked (100 pct). The computed overall stress-strain response varies only slightly when the crack tip is at the particle matrix interface, $a = r_0$. (Note that for the axisymmetric cell model with $a = r_0$, Figure 15, there is a larger difference between the overall stress-strain curves for 0 and 100 pct fractions of cracked particles.) For a slightly longer crack, extending into the matrix $a = 1.004r_0$ in Figure 18, there is a greater sensitivity to the fraction of cracked particles. The aggregate Young's modulus decreases linearly with the fraction of cracked particles. The calculated values of the apparent plane strain stiffness are 102.6, 86.8, and 71.5 GPa for 0, 50, and 100 pct cracked particles, respectively. On the other hand, after extensive yielding, the variation of Σ_{ave}, at a given overall strain ε_{ave} is nonlinear. When the fraction of cracked particles is 50 pct the stress strain curve is reduced from that for intact particles by about one-third of the difference between the stress-strain curves for intact particles and for all particles cracked. The overall strain-hardening rates for the 50 and 100 pct fractions of cracked particles are, however, the same.
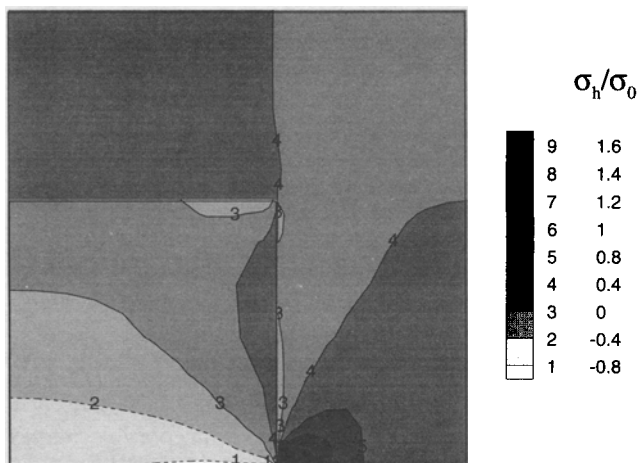
B. Quasi-Static Crack Growth

In the following, the crack is permitted to grow quasi-statically through the particle and then into the matrix or along the particle matrix interface. Crack growth in the
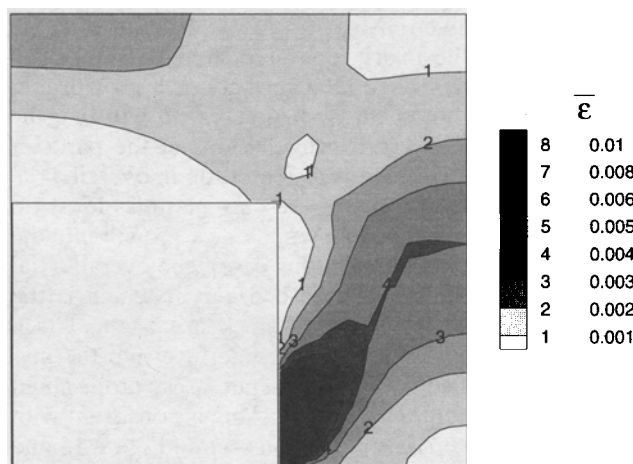
particle and in the matrix is confined to the $y^2 = 0$ plane. The surface along which the crack grows is characterized by Eqs. [11] through [14], with different interface parameters for the three possibilities. Crack propagation into the matrix and along the particle matrix interface is illustrated in Figure 19.

Figure 19(a) shows overall axial stress strain curves for a composite unit cell with a crack that propagates into the matrix. Thus, these stress strain curves are for composites in which every particle has an identical crack. The shape of the particle is a truncated cylinder and initial penny-shaped crack radii of $a = 0.31r_0$, $a = 0.61r_0$, and $a = r_0$ are considered. The calculations are carried out for $\sigma_R^{max} = 1.0$ GPa, $\delta_R = 0.00083R_0$ and $\sigma_M^{max} = 800$ MPa, $\delta_M = 0.0021R_0$, and with the particle-matrix interface taken to be nearly perfectly bonded ($\sigma_{int}^{max} = \tau_{int}^{max} = 10$ GPa) so that there is no interfacial decohesion. Results are also shown where the reinforcement cohesive properties are given by $\sigma_R^{max} = 500$ MPa and $\delta_R = 0.00083R_0$ and the matrix cohesive strength is taken to be very large, $\sigma_M^{max} = 10$ GPa so that crack growth into the matrix does not occur. When crack growth into the matrix is precluded crack growth stops at the particle-matrix interface and there is a small drop in overall axial stress, Σ_{ave} of about 6 pct of the current stress level (in this calculation $a = 0.61r_0$). When crack growth into the matrix occurs ($a = 0.31r_0$ in this case), the overall axial stress level approaches the dashed curve, which is the same computation with the initial crack size $a = r_0$. Crack growth across the particle-matrix interface into the matrix is accompanied by a much larger stress drop, about 35 pct of the current level of Σ_{ave}. This is consistent with the sensitivity to crack-tip location seen in Figure 15 and 18. However, once some crack growth into the matrix occurs, the overall axial stress level is nearly independent of the size of the initial crack within the particle. The contour plot of effective plastic strain, $\bar{\varepsilon}$, in Figure 19(b) shows details of the distribution near the particle matrix interface (the case shown in Figure 19(b) is one for which the particle matrix interface is nearly perfectly bonded, $\sigma_{int}^{max} = 10$ GPa). Other calculations have been carried out considering debonding of the particle-matrix interface rather than propagation of the crack into the matrix, as illustrated in Figure 19(c). In this case, there is a drop in Σ_{ave} accompanying decohesion of the particle-matrix interface which is also about 35 pct of the current overall axial stress level for the case in Figure 19(c). In fact, the magnitude of the stress drop was found to depend primarily on the value of the strain at which the crack reaches the particle-matrix interface. In particular, the magnitude of the stress drop was found to be relatively insensitive to whether crack growth proceeded into the matrix, as in Figure 19(b), or along the particle-matrix interface, as in Figure 19(c). When debonding of the particle-matrix interface occurred, the subsequent overall axial stress-strain response exhibited the same independence of the size of the initial crack, as seen in Figure 19(a).

As seen previously, the fracture of a particle depends strongly on its shape. Furthermore, particle shape also has an effect on the overall constitutive behavior of the composite before and after fracture of the reinforcement.

(a)

σ_h/σ_0

9	1.6
8	1.4
7	1.2
6	1
5	0.8
4	0.4
3	0
2	-0.4
1	-0.8

(b)

$\bar{\varepsilon}$

8	0.01
7	0.008
6	0.006
5	0.005
4	0.004
3	0.003
2	0.002
1	0.001

Fig. 16—Computed contour plots for the Al-3.5 wt pct Cu alloy reinforced with 20 vol pct unit cylinder particles at $\varepsilon_{ave} = 0.005$ with penny-shaped cracks extending slightly into the matrix ($a = 1.001$ r_0): (a) normalized mean normal stress, σ_h/σ_0, and (b) effective plastic strain, $\bar{\varepsilon}$. The tensile axis is vertical.

Fig. 17—Curves of overall axial stress, Σ_{ave} (in MPa), vs overall axial strain, ε_{ave}, for unit cylinder-reinforced composites with various matrix strain-hardening exponents, N, for $a = r_0$ and $a = 1.001$ r_0. All other properties are those of the Al-3.5 Cu/20 pct SiC model system.

Fig. 18—Curves of overall axial stress, Σ_{ave} (in MPa), vs overall axial strain, ε_{ave}, for plane strain model composites with 20 area pct reinforcement with various fractions of cracked particles: 0 (all particles intact), 50, and 100 pct (all particles cracked); and with two crack sizes: $a = r_0$ and $a = 1.004$ r_0. The matrix properties are those of the Al-3.5 wt pct Cu alloy and the elastic reinforcement properties are those specified for SiC. The crack is considered stationary and the particle-matrix interface is taken to be perfectly bonded.

In a parallel study by Shen et al.,[28] a detailed investigation of reinforcement shape effects was carried out, and it was found that abrupt reinforcement corners play a significant role on the aggregate plastic flow response. Here, calculations are carried out simulating crack propagation in a unit cylinder (Figure 1(b)) and in a truncated cylinder Figure 1(c). In both cases, the radius of the initial penny-shaped crack is taken to be $0.2R_0$. The particle-matrix interface and matrix cohesive properties are taken to be identical to those specified at the beginning of Section V. The reinforcement cohesive characteristics are given by $\sigma_R^{max} = 500$ MPa and $\delta_R = 0.00083R_0$. Figure 20 shows contours of mean normal stress and effective plastic strain at $\varepsilon_{ave} = 0.02$. The plastic strain fields reveal a key difference; for the truncated cylinder, there is a band of deformation along the oblique part of the particle-matrix interface with a reduction in the deformation emanating from the crack tip.

In the discussion of Figure 11 in Section V, the focus was on crack growth through the reinforcement. As noted
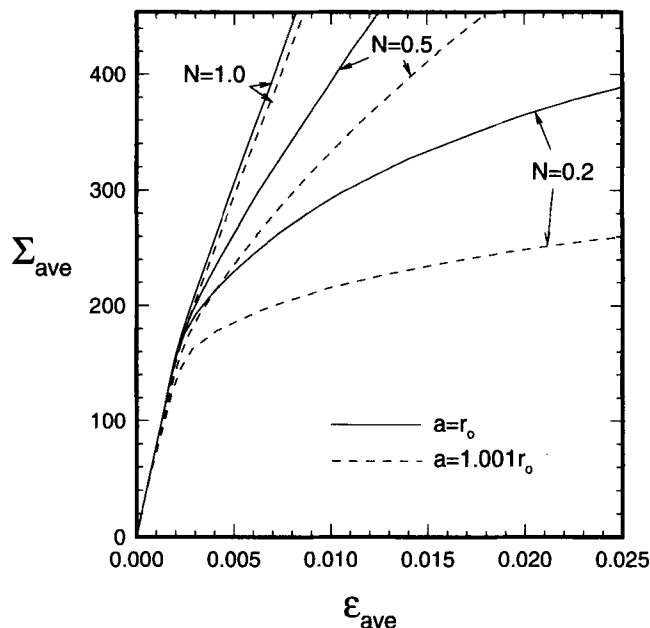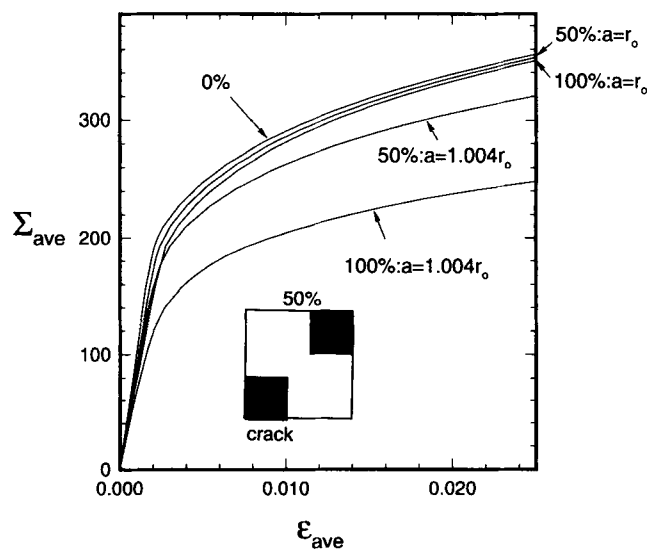
previously, the curves or overall stress, Σ_{ave}, vs overall strain, ε_{ave}, after crack growth through the particle (and somewhat into the matrix) are nearly independent of the initial size of the crack within the reinforcement. This is not necessarily the case for the second drop in the overall stress-strain curves, which is associated with crack growth through the matrix. For the unit cylinder reinforcement (Figure 11(a)), the second drop in Σ_{ave} occurs at $\varepsilon_{ave} \approx$
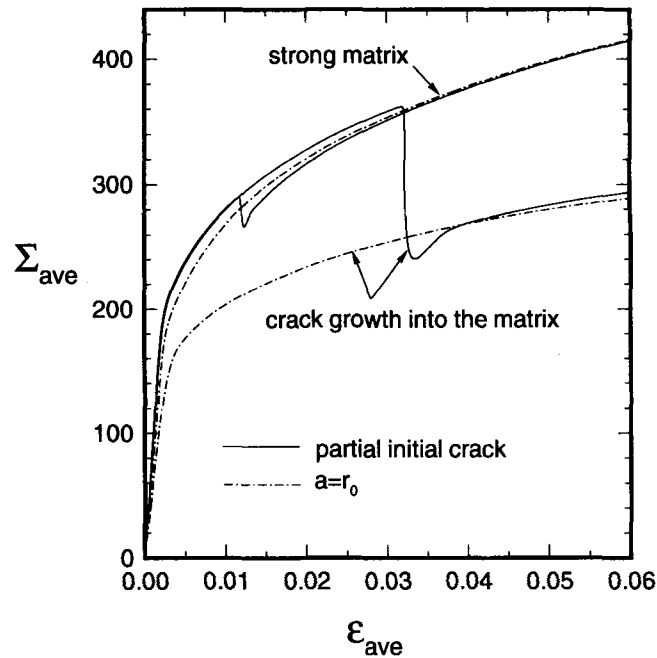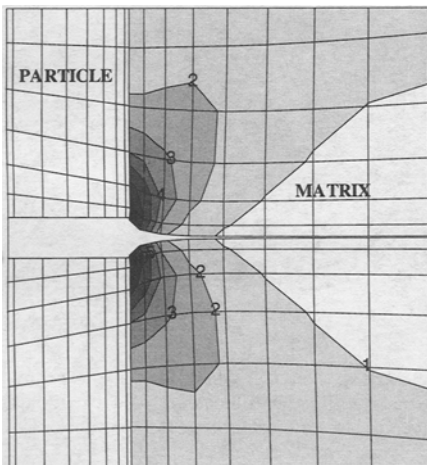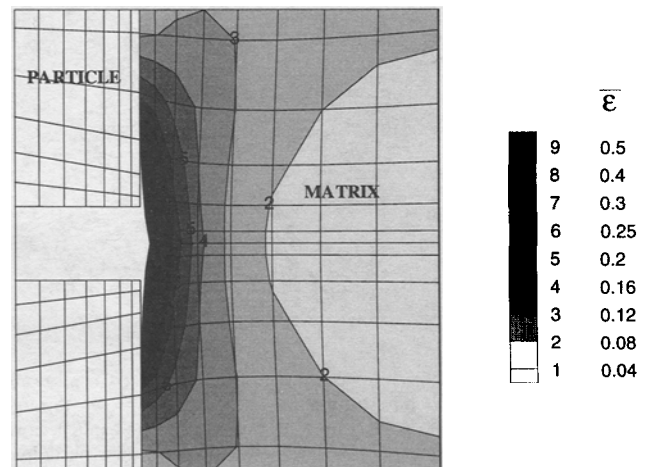
Fig. 19—(a) Curves of overall axial stress, Σ_{ave} (in MPa), vs overall axial strain, ε_{ave}, for the Al-3.5 wt pct Cu alloy reinforced with 20 vol pct truncated cylinder particles showing the effect of the matrix cohesive strength on the behavior. The particle-matrix interface is taken to be early perfectly bonded, and the reinforcement and matrix cohesive properties are specified in the text. The partially cracked particles have initial penny-shaped cracks with $a = 0.31\, r_0$ or $a = 0.61\, r_0$. For comparison purposes, overall axial stress-strain curves for identical composites with $a = r_0$ are shown; (b) computed contours of effective plastic strain, $\bar{\varepsilon}$, when the crack propagates into the ductile matrix at $\varepsilon_{ave} = 0.04$; and (c) computed contours of effective plastic strain, $\bar{\varepsilon}$, when the crack propagates along the particle-matrix interface at $\varepsilon_{ave} = 0.07$. In (b) and (c), a region near the current crack tip is shown that is symmetric about the y^1-axis, although calculations are carried out only for $y^2 \geq 0$. The tensile axis is vertical.

0.02, and this value is relatively insensitive to the size of the initial crack. On the other hand, for the truncated cylinder reinforcement (Figure 11(b)), there is greater dependence on the size of the initial crack, with the second drop in Σ_{ave} occurring earlier for larger initial cracks.

Figure 21(a) shows contours of effective plastic strain for the composite with the truncated cylinder reinforcement and with $a = 0.61r_0$ at $\varepsilon_{ave} = 0.01$, which is shortly after the crack has grown through the reinforcement. The reinforcement cohesive surface is characterized by $\sigma_R^{max} = 500$ MPa and $\delta_R = 0.00083R_0$ and the other parameters are as specified in Section V. For comparison,

Figure 21(b) shows effective plastic strain contours for a similar calculation with $a = r_0$. A band of deformation along the oblique part of the particle-matrix interface is seen only in Figure 21(a), where the initial radius of the penny-shaped crack is $a = 0.61r_0$. In Figure 21(b), where $a = r_0$, plastic flow is concentrated near the crack tip. Prior to crack growth in the matrix, the matrix stress and strain distributions are very different in these two cases. Thus, when the crack does extend into the matrix, the matrix-hardening states differ for the two initial crack sizes, so that the course of crack growth in the matrix and the onset of the sharp drop in Σ_{ave} associated with
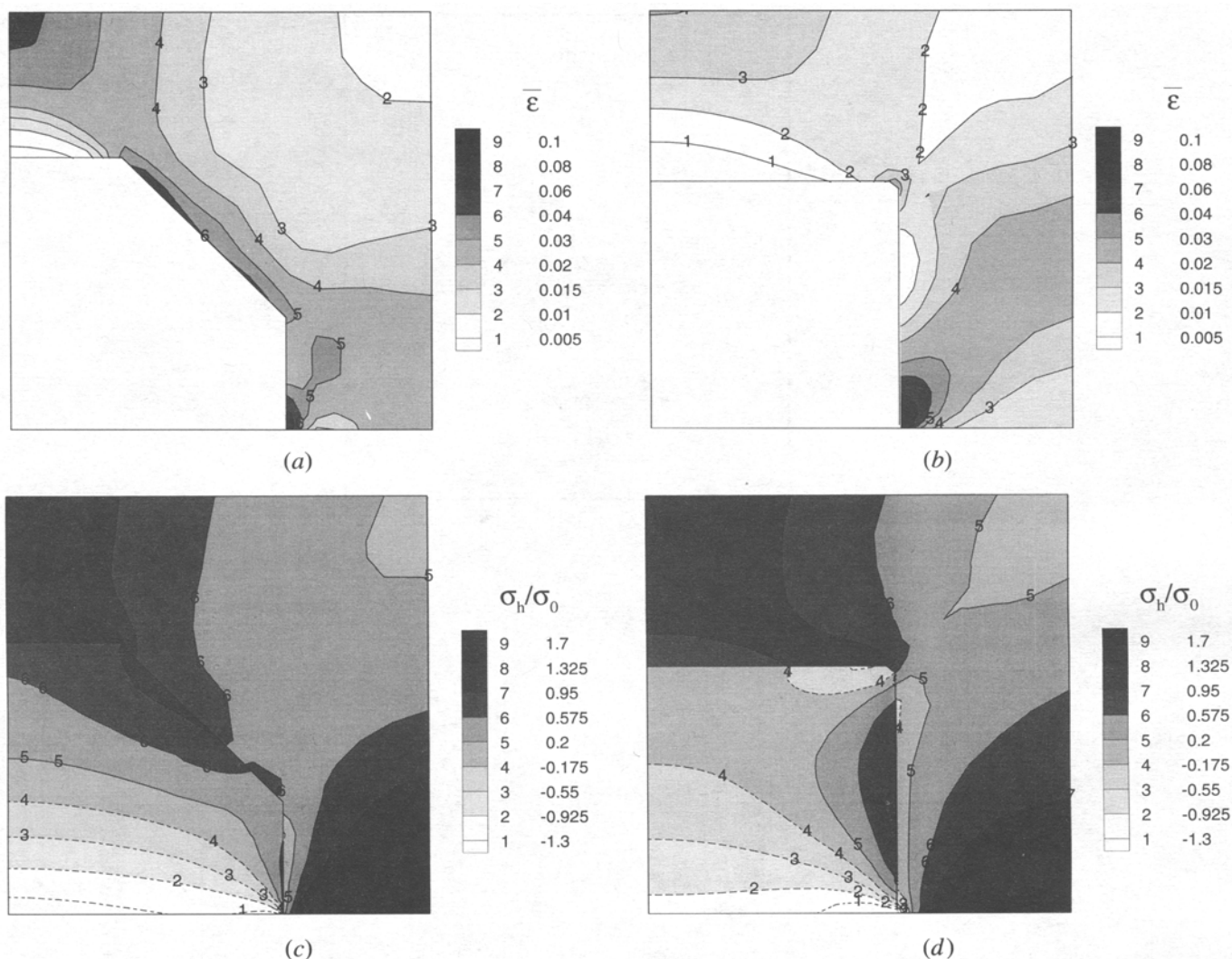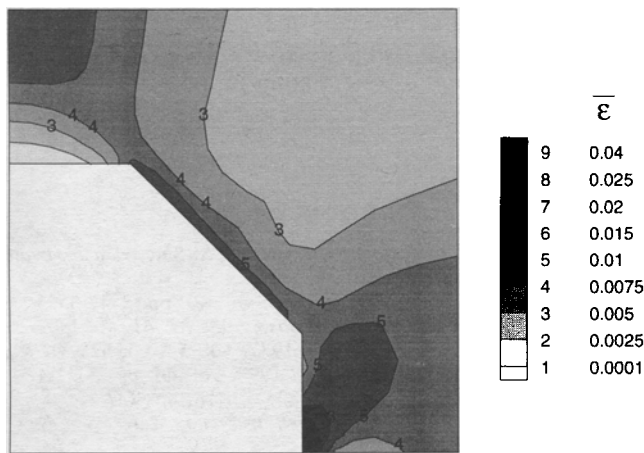
Fig. 20—Computed contour plots for the Al-3.5 wt pct Cu alloy reinforced with 20 vol pct particles at $\varepsilon_{ave} = 0.02$, which is after the penny-shaped crack, which has initial radius $a = 0.2\,R_0$, has grown through the particle: (a) effective plastic strain, $\bar{\varepsilon}$, for truncated cylinder particles; (b) effective plastic strain, $\bar{\varepsilon}$, for unit cylinder particles; (c) normalized mean normal stress, σ_h/σ_0, for truncated cylinder particles; and (d) normalized mean normal stress σ_h/σ_0, for unit cylinder particles. The tensile axis is vertical.

crack growth through the matrix are different in these two cases. Similar behavior has been seen for calculations carried out with a stronger matrix, $\sigma_M^{max} = 600$ MPa. The only difference is that with $\sigma_M^{max} = 600$ MPa, the sharp drop in Σ_{ave} associated with crack growth through the matrix occurs later, at $\varepsilon_{ave} \approx 0.06$.

In these calculations, the cohesive strength in the particle has been taken to be unrealistically small. Figure 22 shows the variation in overall stress-strain response with reinforcement cohesive strength, σ_R^{max}. The particle is a truncated cylinder with an initial penny-shaped crack having $a = 0.31r_0$. The matrix cohesive strength is specified by $\sigma_M^{max} = 600$ MPa and $\delta_M = 0.0021R_0$. Three values of the reinforcement cohesive strength, σ_R^{max}, are considered: 440 MPa with $\delta_R = 0.0010R_0$, 875 MPa with $\delta_R = 0.00052R_0$, and 1750 MPa with $\delta_R = 0.00026R_0$. The value of δ_R is chosen so that the cohesive energy in the three cases is the same. Taking $R_0 = 5.0\ \mu$m, this value corresponds to a tensile cohesive energy, ϕ_n, of 6.2 J/m^2. The particle-matrix interfaces considered in these calculations are $\sigma_{int}^{max} = 500$ MPa, $\sigma_{int}^{max} = 800$ MPa,

and $\sigma_{int}^{max} = 10$ GPa (a nearly perfectly bonded interface). The remaining parameters characterizing the particle-matrix interface are kept fixed at the values used in the previous calculations. With $\sigma_R^{max} = 440$ MPa, the strength of the particle-matrix interface has nearly no effect, and in all three calculation reinforcement cracking occurs at $\varepsilon_{ave} = 0.006$ and the second sharp drop in Σ_{ave} at around $\varepsilon_{ave} = 0.06$. For the three calculations with $\sigma_R^{max} = 875$ MPa, reinforcement cracking occurs at around $\varepsilon_{ave} = 0.02$ and particle fracture is associated with a decrease in ε_{ave}. A similar response occurs for the case with $\sigma_R^{max} = 1750$ MPa, with the nearly perfectly bonded particle interface ($\sigma_{int}^{max} = 10$ GPa), with particle cracking occurring at $\varepsilon_{ave} = 0.09$. Such strain reversal is characteristic of high-strength, brittle interfaces.[4] The actual behavior would be dynamic, and realistic characterizations of particle fracture would need to account for inertial effects. For $\sigma_R^{max} = 1750$ MPa and for both $\sigma_{int}^{max} = 500$ MPa and $\sigma_{int}^{max} = 800$ MPa, debonding of the particle-matrix interface occurs before crack growth in the particle and lowers the stress in the reinforcement so

(a)
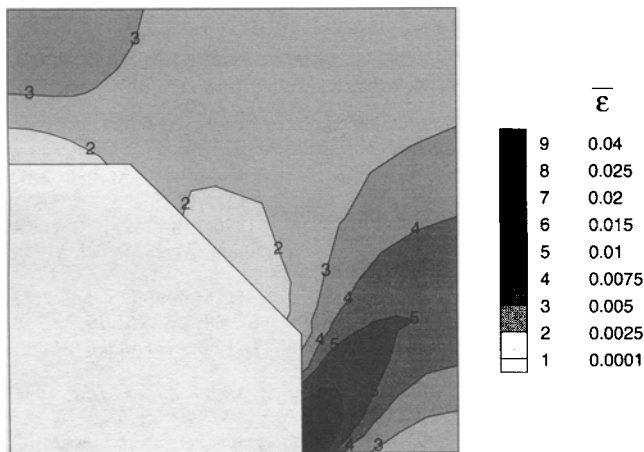
(b)

Fig. 21—Computed contours of effective plastic strain, $\bar{\varepsilon}$, for the Al-3.5 wt pct Cu alloy reinforced with 20 vol pct truncated cylinder particles at $\varepsilon_{ave} = 0.01$, which is after the crack has grown through the particle: (a) after propagation of a penny-shaped crack with initial radius $a = 0.61\ r_0$ and (b) for a penny-shaped crack with initial radius $a = r_0$. The tensile axis is vertical. The matrix strength is given by $\sigma_M^{max} = 400$ MPa and $\delta_M = 0.0021\ R_0$.

Fig. 22—Curves of overall axial stress, Σ_{ave} (in MPa), vs overall axial strain, ε_{ave}, with various values of the strength of the particle-matrix interface and various characterizations of the reinforcement cohesive properties. The reinforcement is a truncated cylinder, and there is an initial penny-shaped crack with radius $a = 0.31\ r_0$. Further details are given in the text.

that partial fracture does not occur, at least over the strain range considered.

VII. CONCLUSIONS

1. Finite element simulations of particle fracture in metal-matrix composites have been carried out. The results of these analyses provide a mechanistic justification for a variety of experimentally observed trends in aluminum alloys reinforced with SiC particles. Specifically, parametric analyses of reinforcement fracture reported in this work rationalize the effects of particle size, local clustering of particles, reinforcement volume fraction, and mode of applied loading on the propensity for particle fracture.

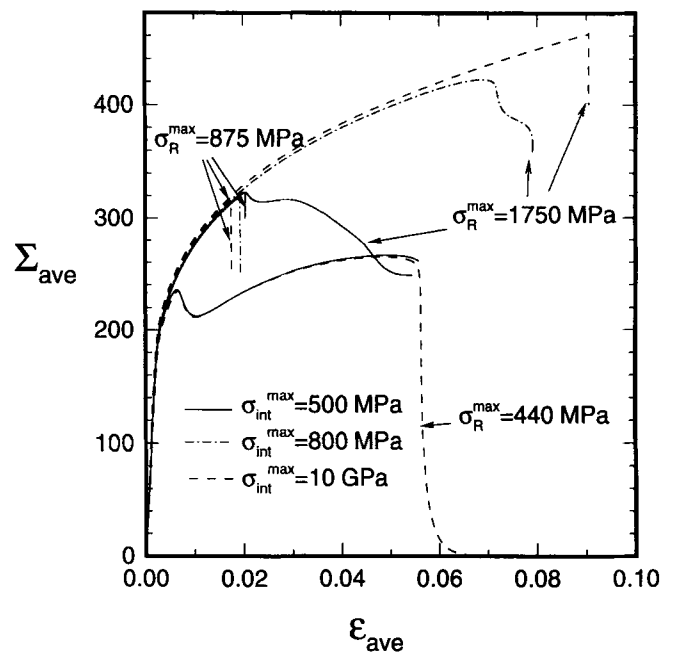2. Particle fracture as well as interfacial decohesion triggered by particle fracture mitigate the buildup of triaxial stresses within the matrix during tensile loading, a consequence of which is a reduced level of overall flow stress.

3. The overall stress-strain response is not very sensitive to the size of a pre-existing flaw embedded within the reinforcing particle provided that the particle is much stiffer than the matrix (as, for example, in the aluminum-SiC composite system).

4. The effects of such factors as interface compliance, particle shape, matrix constitutive response and pre-existing defects within the particle on the overall fracture behavior are modeled using finite element formulations. Furthermore, the onset of cracking within the particle, the evolution of field quantities as the crack propagates quasi-statically within the particle to the particle matrix interface, and the dependence of tensile constitutive response during continued crack advance within the matrix have been analyzed. The trends predicted by these models are consistent with a variety of experimental observations.

LIST OF SYMBOLS*

a	crack length
E_{ij}	covariant components of Lagrangian strain
E	Young's modulus
f_c	volume fraction of fractured particles
L_0	height of the unit cell
m	strain rate hardening exponent of the matrix
N	strain hardening exponent of the matrix
q, r	cohesive constitutive parameters
r_0	radius (or width) of the particle
R_0	radius (or width) of the unit cell
S	area
T^i	nominal traction components
u_i	covariant components of the displacement vector
V_R	volume of the reinforcement
V_{cell}	volume of the unit cell
δ_n, δ_t	cohesive surface length parameters
Δ_i	covariant components of the displacement jump across a cohesive surface
$\dot{\varepsilon}_{ave}$	average axial strain rate
ε_{ave}	average axial strain
ν	Poisson's ratio
$\bar{\varepsilon}$	effective strain
$\dot{\bar{\varepsilon}}$	effective strain rate
σ_0	yield strength of the matrix
σ_h	hydrostatic stress
$\bar{\sigma}$	effective stress
Σ_{ave}	overall average axial stress
Σ_R	average axial stress in the reinforcement
σ^{max}	strength for normal separation of a cohesive surface
τ^{max}	strength for tangential separation of a cohesive surface
τ	Kirchhoff stress
$\hat{\tau}$	Jaumann rate of Kirchhoff stress
τ'	deviatoric Kirchhoff stress
ϕ	cohesive surface potential
ϕ_n	work of separation for normal decohesion
ϕ_t	work of separation for tangential decohesion
*	Unless explicitly specified the following conventions are adopted
$(\ )_R$	pertaining to the reinforcement
$(\ )_M$	pertaining to the matrix
$(\ )_{int}$	pertaining to the reinforcement matrix interface
$(\ )_n$	normal component of a vector
$(\ )_t$	tangential component of a vector
$(\ )_{,i}$	covariant differentiation in the reference frame

REFERENCES

1. Y.L. Shen, M. Finot, A. Needleman, and S. Suresh: *Acta Metall. Mater.*, 1994, vol. 42, pp. 77–97.
2. G. Bao: *Acta Metall. Mater.*, 1992, vol. 40, pp. 2547-55.
3. V. Tvergaard: *J. Mech. Phys. Solids*, 1993, vol. 41, pp. 1309-26.
4. A. Needleman: *J. Appl. Mech.*, 1987, vol. 54, pp. 525-31.
5. A. Needleman: *Ultramicroscopy*, 1992, vol. 40, pp. 203-14.
6. V. Tvergaard: *Int. J. Fract.*, 1982, vol. 18, pp. 237-52.
7. X. Xu and A. Needleman: *Modelling Simul. Mater. Sci. Eng.*, 1993, vol. 1, pp. 111-32.
8. J. Llorca, A. Needleman, and S. Suresh: *Acta Metall. Mater.*, 1991, vol. 39, pp. 2317-35.
9. J. Llorca, S. Suresh, and A. Needleman: *Metall. Trans. A*, 1992, vol. 23A, pp. 919-34.
10. S. Suresh, T. Christman, and Y. Sugimura: *Scripta Metall.*, 1989, vol. 23, pp. 1599-1602.
11. J.W. Hutchinson: in *Numerical Solution of Nonlinear Structural Problems*, R.F. Hartung, ed., ASME, New York, NY, 1973, p. 17.
12. A. Needleman: in *Plasticity of Metals at Final Strain: Theory, Experiment and Computation*, E.H. Lee and R.L. Mallett, eds., RPI press, Troy, NY, 1982, pp. 387-436.
13. V. Tvergaard: *J. Mech. Phys. Solids*, 1976, vol. 24, pp. 291-304.
14. D. Peirce, C.F. Shih, and A. Needleman: *Comp. Struct.*, 1984, vol. 18, pp. 857-87.
15. J. Yang, C. Cady, M.S. Hu, I. Zok, R. Mehrabium, and A.G. Evans: *Acta Metall. Mater.*, 1990, vol. 38, pp. 261-19.
16. Y. Brechet, J.D. Embury, S. Tao, and L. Luo: *Acta Metall. Mater.*, 1991, vol. 39, pp. 1781-86.
17. T. Mochida, M. Taya, and D. Lloyd: *Mater. Trans. JIM*, 1991, vol. 32, pp. 931-42.
18. P.M. Mummery, P. Anderson, G. Davis, B. Derby, and J.C. Elliott: *Scripta Metall. Mater.*, 1993, vol. 29, pp. 1457-62.
19. P.M. Mummery, B. Derby, and C.B. Scruby: *Acta Metall. Mater.*, 1993, vol. 41, pp. 1431-45.
20. J. Bonnen, J. Allison, and J.W. Jones: *Metall. Trans. A*, 1991, vol. 22A, pp. 1007-19.
21. C.L. Hom: *J. Mech. Phys. Solids*, 1992, vol. 20, pp. 991-1008.
22. M.S. Hu: *Scripta Metall. Mater.*, 1991, vol. 25, pp. 695-700.
23. G.M. Newaz and B.S. Majumdar: *J. Mater. Sci. Lett.*, 1993, vol. 12, pp. 551-52.
24. W.H. Hunt, Jr., J.R. Brockenbrough, and P.E. Magnusen: *Scripta Metall. Mater.*, 1991, vol. 25, pp. 15-20.
25. H. Ribes, R. Da Silva, M. Suéry, and T. Bretheau: *Mater. Sci. Technol.*, 1990, vol. 6, pp. 621-28.
26. Y. Brechet, J. Newell, S. Tao, and J.D. Embury: *Scripta Metall. Mater.*, 1993, vol. 28, pp. 47-52.
27. J.R. Rice: *J. Appl. Mech.*, 1968, vol. 35, pp. 379-86.
28. Y.-L. Shen, M. Finot, A. Needleman, and S. Suresh: Brown University, Providence, RI, unpublished research, 1994.